Stability and structure of platinum sulfide complexes in hydrothermal fluids

C. Laskar, E.F. Bazarkina, M.A. Kokh, Jean-Louis F Hazemann, R. Vuilleumier, E. Desmaele, G. Pokrovski

Journal Pre-proofs

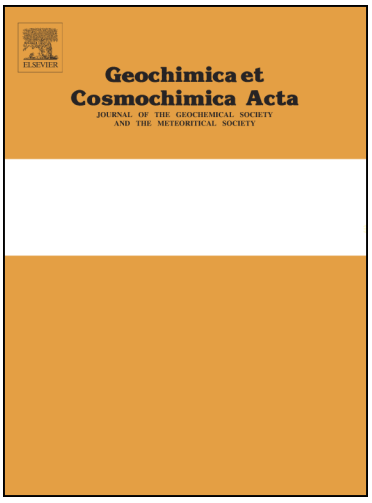

Stability and structure of platinum sulfide complexes in hydrothermal fluids

C. Laskar, E.F. Bazarkina, M.A. Kokh, J.-L. Hazemann, R. Vuilleumier, E. Desmaele, G.S. Pokrovski

PII: S0016-7037(22)00397-0
DOI: https://doi.org/10.1016/j.gca.2022.08.015
Reference: GCA 12748

To appear in: *Geochimica et Cosmochimica Acta*

Received Date: 25 April 2022
Revised Date: 3 August 2022
Accepted Date: 12 August 2022

Please cite this article as: Laskar, C., Bazarkina, E.F., Kokh, M.A., Hazemann, J.-L., Vuilleumier, R., Desmaele, E., Pokrovski, G.S., Stability and structure of platinum sulfide complexes in hydrothermal fluids, *Geochimica et Cosmochimica Acta* (2022), doi: https://doi.org/10.1016/j.gca.2022.08.015

Stability and structure of platinum sulfide complexes in hydrothermal fluids

C. Laskar[1], E.F. Bazarkina[2, 4, 5], M.A. Kokh[1], J.-L. Hazemann[2], R. Vuilleumier[3], E. Desmaele[3], and G.S. Pokrovski[1]

[1]Géosciences Environnement Toulouse (GET), UMR 5563, Centre National de la Recherche Scientifique (CNRS), Observatoire Midi-Pyrénées, Université Paul Sabatier Toulouse III, Institut de Recherche pour le Développement (IRD), 14, avenue Edouard Belin, F-31400 Toulouse, France
[2]Institut Néel, UPR 2940 CNRS, Grenoble, France Univ. Grenoble Alpes, 25, avenue des Martyrs, F-38042 Grenoble Cedex 9, France
[3]École Normale Supérieure - PSL Research University, Département de Chimie, Sorbonne Universités - UPMC Univ Paris 06, CNRS UMR 8640 PASTEUR, 24, rue Lhomond, F-75005 Paris, France
[4]Institute of Resource Ecology, Helmholtz Zentrum Dresden-Rossendorf (HZDR), PO Box 510119, 01314 Dresden, Germany
[5]The Rossendorf Beamline at ESRF, The European Synchrotron, CS40220, 38043 Grenoble Cedex 9, France

*Correspondence: Clément Laskar (clement.laskar@gmail.com)

ABSTRACT

Knowledge of the chemical speciation of platinum and the solubility of Pt-bearing minerals in hydrothermal fluids is required to assess Pt transport, remobilization and concentration in the Earth's crust. In this study, we combined PtS(s) solubility measurements in a hydrothermal reactor allowing fluid sampling, in situ X-ray absorption spectroscopy, and first-principles molecular dynamics simulations to systematically investigate the structure, composition and stability of Pt sulfide complexes in model aqueous H_2S-bearing solutions up to 300 °C and 600 bar. The results demonstrate that tetrahydrosulfide, $Pt^{II}(HS)_4^{2-}$, is the major Pt-bearing complex in aqueous solutions saturated with PtS(s) over a wide range of dissolved hydrogen sulfide concentrations, from <0.2 to ~2 molal. The equilibrium constants of the dissolution reaction of PtS(s) generated in this study, $PtS_{(s)} + 3\ H_2S_{(aq)} = Pt(HS)_4^{2-} + 2\ H^+$ (β_4), are described by the equation $\log_{10}\beta_4 = 0.9\times1000/T(K) - 19.7$ (±0.5) over the temperature range 25–300 °C and pressure range P_{sat}–600 bar. Furthermore, the stepwise formation constants of four Pt^{II}-HS complexes, $Pt(HS)^+$, $Pt(HS)_2^0$, $Pt(HS)_3^-$, and $Pt(HS)_4^{2-}$, were estimated, for the first time, from molecular dynamics simulations. The generated constants indicate that the maximum solubility of platinum in the form of $Pt(HS)_4^{2-}$ in reduced H_2S-dominated hydrothermal fluids at moderate temperatures (≤350 °C) is close to 1 ppb Pt at near-neutral pH of 6–8 and hydrogen sulfide concentrations of 0.1 molal. Although this solubility is much greater than that of Pt-Cl, Pt-OH and Pt-SO_4 complexes at such conditions, it is yet too low to account for significant Pt transport in most shallow-crust hydrothermal settings, characterized by the presence of both sulfide and sulfate. Complexes with S-bearing ligands, very likely other than H_2S/HS^-, such as S_3^-, would be required to account for Pt hydrothermal mobility. Our results provide a basis for more systematic future studies, using combined approaches, of the role of hydrothermal fluids in the behavior of platinum group elements in nature.

Keywords: platinum sulfide complexes, hydrothermal fluid, solubility, X-ray absorption spectroscopy, molecular dynamics, stability constant.

Platinum-group elements (PGEs; Ru, Rh, Pd, Os, Ir, and Pt) are eagerly sought critical metals for many technological fields, spanning from the automotive and petrochemical industries to pharmaceutics and nanomaterials. Among these metals, platinum is one of the most largely used (e.g., Ahmadi et al., 1996; Moldovan et al., 2002; Lee et al., 2008; Kim et al., 2015; Chong et al., 2018). Platinum is, however, a trace element in nature, with average concentrations of <1 ppb in the upper continental crust (Chen et al., 2016), and its deposits are very scarce. The majority of actually known economic Pt concentrations comes from (ultra)mafic magmatic settings where Pt and other PGE are concentrated along with Fe-Ni-Cu sulfide minerals and melts, such as Bushveld, Norilsk and Sudbury that account for >95% of economic platinum extraction (Mungall and Naldrett, 2008; Barnes and Liu, 2012; Mudd and Jowitt, 2014; Barnes et al., 2017). Platinum is intimately associated with reduced sulfur in such settings, being concentrated in pentlandite ($(Fe,Ni)_9S_8$), chalcopyrite ($CuFeS_2$), and pyrrhotite (FeS_{1+x}, $x<0.1$), both in the form of solid solutions and individual Pt-bearing mineral phases such as platinum metal (Pt) and its alloys, sulfides ($Pt^{II}S$ and $Pt^{IV}S_2$), selenides (e.g., $PtSe_2$), arsenide ($PtAs_2$), telluride ($PtTe_2$), stanides (PtSn), bismuthides ($PtBi_2$), and antimonides ($PtSb_2$), to name a few (Mcmahon et al., 1997; Hanley, 2005; Hutchinson and Kinnaird, 2005; Zientek, 2012; O'Driscoll and González-Jiménez, 2016; Duran et al., 2017). In these and most other solids, Pt usually occurs in three formal oxidation states, 0, II and IV. The mechanisms of Pt concentration in magmatic deposits are believed to be controlled by different processes of fractional crystallization, fractionation and segregation of silicate and sulfide melts (e.g., Kerr and Leitch, 2005; Brenan, 2008; Lorand et al., 2008; Palme, 2008). However, the potential role of aqueous magmatic or post-magmatic fluids in PGE concentration and remobilization processes in such deposits is constantly debated in the literature

(e.g., Kanitpanyacharoen and Boudreau, 2013; Le Vaillant et al., 2016a,b; Boudreau, 2019; Sullivan, 2022a,b). In parallel, there are numerous instances of (re)mobilization and concentration of Pt, as well as other PGE, in various hydrothermal settings such as porphyry Cu-Au-Mo, black-shale hosted gold

deposits, and serpentinites from subduction zones (Ballhaus and Stumpfl, 1986; Rehkämper et al., 1997; Wood and Cabri, 2002; Mungall, 2005; Luguet et al., 2008; Arai and Miura, 2016; Barnes and Ripley, 2016; Boudreau, 2019), with Pt concentrations locally reaching up to 3 orders of magnitude more than its average crustal abundance. These observations point to an important, but often overlooked so far, the role of moderate-temperature (200–500 °C) hydrothermal fluids in Pt transport. Such hydrothermal settings may become potentially exploitable for PGE in the near future. Therefore, knowledge of Pt chemical speciation and solubility in the hydrothermal fluid phase is required to quantify the formation and distribution of Pt resources in nature as well as to optimize the rapidly growing Pt use in technological processes. Indeed, among the four major types of ligands in natural fluids (hydroxide, chloride, sulfate and sulfide), the "soft" nature of sulfide species (H_2S, HS^-, S^{2-}) makes them the most plausible candidates for binding the "soft" platinum cations (Pt^{2+}, Pt^{4+}), according to the HSAB theory (Hard and Soft Acids and Bases; Pearson, 1968a,b, 1997). The present study is devoted to a systematic determination of the nature, stability and geological role of Pt sulfide aqueous complexes in shallow-crust hydrothermal fluids.

2. BRIEF OVERVIEW OF AVAILABLE DATA AND APPROACHES USED IN THIS STUDY

The rare studies of Pt sulfide type complexes at hydrothermal conditions are both inconsistent and controversial. This is because all of them employed the bulk solubility approach to the PtS(s) and PtS_2(s) solid phases using hydrothermal reactors (Gammons and Bloom, 1993; Pan and Wood, 1994; Kokh et al., 2017; Filimonova et al., 2021; Pokrovski et al., 2021). Such solubility experiments are

intrinsically difficult to perform and interpret both because of the low, often ppb-level, Pt dissolved concentrations posing severe analytical challenges, and the narrow pH and sulfur concentration ranges that may practically be covered by such experiments. These issues often make it ambiguous the

derivation of Pt complex stoichiometries from the analysis of Pt bulk solubility dependence on those parameters. For example, Gammons and Bloom (1993) measured PtS(s) solubility in H_2S/HS^- solutions (pH 0.5–8.4, 0.4–1.0 m S; where m is molality, mol/kg H_2O, throughout the article) from 200 to 300 °C under saturated vapor pressure (P_{sat}) using fused silica tubes quenched at the end of experiment. Their interpretation suggests three Pt complexes, $Pt(HS)_2^0$, $Pt(HS)_3^-$ and $Pt(HS)_4^{2-}$, among which di- and trihydrosulfide would be the most abundant. However, their solubility-pH-H_2S trends were quite scattered to allow robust constraints on the exact Pt species ligation number. Their study contrasts with that of Pan and Wood (1994) who used H_2S/SO_4^{2-} solutions of comparable pH and sulfide concentration ranges (pH 5.9–9.4; 0.3–2.2 m S) to measure PtS/PtS_2 solubility from 200 to 350 °C at P_{sat} using hydrothermal reactors allowing fluid sampling. Pan and Wood (1994) tentatively assumed $Pt(HS)_2^0$ to be the major species. However, they failed to provide enough constraints on its stoichiometry and, therefore, proposed to the reader a large choice of alternative complexes (from $Pt(HS)^+$ to $Pt(HS)_4^{2-}$) with their corresponding formation constants. The absolute PtS(s) solubility values predicted using Pan and Wood's (1994) stability constants are, however, 3 to 4 orders of magnitude higher than those from Gammons and Bloom (1993) at the same temperature and solution compositions. Kokh et al. (2017) used a flexible-cell reactor to measure PtS(s) solubility in supercritical H_2O-CO_2 fluids with pH and redox buffered by aluminosilicate and sulfide/oxide iron mineral assemblages at 450 °C and 650–750 bar (pH=4–6, 0.02–0.06 m S). The authors demonstrated the predominance of the uncharged $Pt(HS)_2^0$ complex with equilibrium concentrations of 1–2 ppb, which were 100 times lower than those predicted by extrapolating Pan and Wood's (1994) data to 450 °C. More recently, Filimonova et al. (2021) measured PtS(s) solubility in dilute H_2S/HS^- solutions (pH=3–8, 0.01–0.2 m S) at 50–75 °C, 1 bar, and at 450 °C, 1000 bar, using batch reactors quenched at the run

end. They tentatively interpreted their data by $Pt(HS)_2^0$ as the dominant species, with PtS(s) solubility magnitudes matching those of Gammons and Bloom (1993) and Kokh et al. (2017). However, the ppb-level Pt concentrations found might have been subjected to significant uncertainties by the use of a quench technique that often suffers from elevated analytical backgrounds. Finally, Pokrovski et al. (2021) measured PtS(s) solubility in sulfate-sulfide bearing solutions containing significant concentrations of the trisulfur radical ion S_3^- within a narrow *T-P* and S concentration range (275–300 °C, 500–700 bar, 1–2 m S) using different types of hydrothermal reactors (both quench- and sampling-based) as well as in situ X-ray absorption spectroscopy. Their data show that the presence of S_3^- enhanced Pt solubility by 3 to 5 log units compared to H_2S-dominated solutions, due to the formation of mixed $Pt\text{-}HS^-\text{-}S_3^-$ species. However, the results of Pokrovski et al. (2021) might be dependent on the choice of data for Pt-HS complexes dominant in S_3^-– free solutions. This brief overview highlights that far more systematic data are required to constrain the nature and stability of Pt sulfide complexes, which is unlikely to be achieved using solely bulk-solubility approaches.

In the last 10 years, significant progress of in situ spectroscopic and molecular modeling approaches has provided unprecedented support to traditional bulk-solubility batch-reactor experiments for investigating metal complexation in hydrothermal fluids. In particular, X-ray absorption spectroscopy (XAS) has emerged as the most direct approach to obtain information about the metal oxidation state and coordination, the identity of its ligands in chemical complexes, as well as to measure in situ metal dissolved concentrations (Pokrovski et al., 2005, 2006; Bazarkina et al., 2010, 2014; Mei et al., 2015a; Tagirov et al., 2019). Extensive XAS measurements have been performed on various Pt mineral phases and aqueous and surface complexes in both technological and geological materials (e.g., Ayala et al., 2001; Peyrelade, 2005; Crowther, 2007; Gorczyca et al., 2014; Scholten et al., 2018; Tagirov et al., 2019; Filimonova et al., 2019). In contrast, no XAS data are available for sulfur-bearing hydrothermal fluids (with a single exception of Pokrovski et al., 2021, to the best of our knowledge), and Pt-HS complexes have never been directly investigated by XAS. Another rapidly

emerging theoretical method, first-principles molecular dynamics (FPMD) simulations, represents a valuable complementary approach to both solubility and XAS to investigate the structure and stability of metal complexes. In particular, the first-principles thermodynamic integration approach enables

determination of the stepwise formation constants of metal complexes in hydrothermal fluids, as demonstrated for various base and precious metals in S-, Cl- and O- aqueous systems, e.g., U-O-OH-Cl-NO_3 (Bühl et al., 2006, 2008), Cu-HS-Cl (Mei et al., 2013a), Au-HS-S_3 (Mei et al., 2013b), (Au/Cu)-Cl (Mei et al.,2014), Pd-HS-Cl (Mei et al., 2015a), Zn-Cl (Mei et al., 2015b), Au-HS-S_3 (Pokrovski et al., 2015), Zn-HS (Mei et al., 2016), Au-NH_3-OH (Mei et al., 2020), Y-Cl (Guan et al., 2020), and Au-HS-S_3 (Pokrovski et al., 2022).

In this work, we attempted to better quantify the stoichiometry and stability of Pt-HS complexes in hydrothermal fluids through a combination, for the first time in a single study, of three complementary approaches: solubility measurements, in situ XAS experiments, and FPMD simulations. Our results place more robust constraints on both the chemical nature and geological significance of Pt sulfide complexes in hydrothermal fluids, and provide a foundation for future research on metals in hydrothermal fluids and, potentially, silicate melts using combined interdisciplinary approaches.

3. MATERIALS AND METHODS

3.1. Solid phases

Native metal, Pt(s), and platinum sulfides, $Pt^{II}S$(s) and $Pt^{IV}S_2$(s), were used in our solubility and XAS experiments. Both sulfide phases were synthetized by the solid-state method using the protocols of Laskar (2022), by reacting nearly stoichiometric amounts of Pt and S at 750 °C for 10 days in silica tubes sealed under argon atmosphere. Both phases were also used as Pt^{II} and Pt^{IV} structural references in XAS analyses (section 3.3.3). The PtS(s) solid was additionally hydrothermally synthesized according to Kokh et al. (2017), by reacting stoichiometric amounts of Pt and S in a 0.1 m NaOH aqueous solution

placed in a titanium reactor at 450 °C and 500 bar for 11 days. This solid was used in batch-reactor experiment m35 of this study (section 3.3.1). A commercially available platinum metal foil (GoodFellow; 100 µm thickness, 99.95% purity) was used in XAS hydrothermal experiments instead of

PtS(s) powder to avoid an eventual contamination of aqueous solution XAS spectra by the signal from fine solid particles getting dispersed in the solution. The Pt metal foil gets sulfidized very quickly in contact with the sulfur-bearing fluid by forming a strongly adhering homogeneous layer of PtS(s) in equilibrium with the fluid (Pokrovski et al., 2021). For each experiment, a new piece of Pt foil was used to avoid potential cross-contamination; the piece was washed with hot acid (5 wt% HCl + HNO_3 for 30 min) before each experiment to increase its surface roughness and enable more rapid and efficient sulfidation.

To limit the oxidation of the fluid in experiment m35, the mineral buffer pyrite-pyrrhotite (PP), composed of pyrite FeS_2(s) (Aldrich, >99%) and troilite FeS(s) (Aldrich, >95%) was loaded into the reactor, together with the aqueous H_2S-solution whose sulfur concentration was large enough (0.5–1 m) to remain almost constant during equilibration and troilite/pyrrhotite transformation to pyrite. The oxygen fugacity f_{O_2} was therefore controlled by the reaction:

$$FeS_{1+x(s)} + (1–x)\ H_2S_{(aq)} + (1–x)/2\ O_2 = FeS_{2(s)} + (1–x)\ H_2O \qquad (x<0.1) \qquad (1)$$

yielding f_{O_2} values of ~5 orders of magnitude lower than those in a $H_2S/HS^-/SO_4^{2-}$ system. Minor variations in pyrrhotite composition ($x<0.1$) yield negligible oxygen fugacity variations ($\Delta \log f_{O_2}<5\%$) and do not affect the Pt stable phase equilibria at out experimental conditions (Fig. 1). Such redox buffering during our experiment ensures both the thermodynamic stability of PtS(s), as opposed to PtS_2(s) in the presence of sulfate (e.g., Pan and Wood, 1994), and negligibly low concentrations ($<10^{-8}$ m) of polysulfide ions S_n^{2-} ($2 \le n \le 8$) and the S_3^- radical ion that are very strong complexing agents for Pt (e.g., Pokrovski et al., 2021). At temperatures below 250 °C, pyrrhotite tended to be partly consumed

by pyrite; nevertheless, FeS(s) consumption had no significant effect either on aqueous S concentrations or the redox potential, which always remained within the PtS(s) stability field (Fig. 1).

crystallinity. Small amounts (<10%) of PtS_2(s) were found in the initial PtS(s) solid-state synthesized phase, likely due to minor excess of sulfur during the synthesis, but without effect on the solubility which was always controlled by PtS(s). Metallic gold, as the material of the flexible cell of the hydrothermal reactor, was also present in the experiment. Synthetic palladium sulfide, PdS(s), as per Bazarkina et al. (2014), was also added in this experiment. Palladium dissolved concentration were, however, too low (<10 ppm Pd) to modify the composition of the fluid, pH or redox. The analysis of the Pd solubility data will be a subject of future publications.

3.2. Fluid phase

The sources of sulfur in the aqueous solutions used in this study were sodium hydrosulfide (NaHS) and thioacetamide (CH_3CNH_2S). Solutions of NaHS were prepared by bubbling H_2S(g) through a NaOH aqueous solution (1 or 2 m, depending on the experiment) until saturation ($P_{H_2S_{(g)}}$=1 bar). The obtained NaHS solutions were diluted (if necessary) with deoxygenated water and used both in batch-reactor experiment m35 and XAS experiments Exp1 to Exp9 (Tables 1 and 2), with total sulfide concentrations of 0.3–2.2 m. Because NaHS solutions are prone to rapid oxidation yielding polysulfide dianions (S_n^{2-}), their presence was examined by in situ Raman spectroscopy (514.5 nm green laser excitation) in a sapphire cell using the hydrothermal apparatus developed at the Néel Institute (Testemale et al., 2005). The freshly synthesized NaHS solutions (<2 days) were found to be free of polysulfides (detection limit 0.001 m S), from 25 °C to at least 200 °C (P_{sat} to 600 bar). In contrast, a one-year-old NaHS solution showed a bright-yellow coloration and yielded a Raman spectrum with a large peak at 390–510 cm^{-1} at 25 °C/1 bar arising from S_n^{2-} (Trofimov et al., 2009; Pokrovski and

Dubessy, 2015; Steudel and Chivers, 2019). Therefore, extreme care has been taken in this study to use only fresh and uncolored NaHS solutions to avoid any complexation of Pt with the polysulfide ions. In addition, the analyses in our freshly prepared solutions of reduced sulfur concentrations (H_2S/HS^-)

(see section 4.3.1) confirm the absence of polysulfides and EXAFS spectra from our XAS experiments (see section 4.1.2) do not indicate any 2nd shell signals that might arise from polysulfide chains if they were to be bound to Pt. Solution pH was measured using a combination glass electrode, at ambient *T-P* before loading into the reactor or spectroscopic cell, to quantify the amount of H_2S using the dissociation constant:

$$H_2S = H^+ + HS^- \text{ (pK=7.03 at 25 °C, 1 bar)} \quad (2)$$

The value of this constant imposes limitations as to the practical use of NaHS-H_2S solutions at pH <6–7 due to a rapid massive degassing of volatile H_2S molecules whose solubility in water is rather small (<0.1 m at 25 °C, 1 bar). Therefore, to cover the acidic pH region, another sulfur source, thioacetamide, was used. Thioacetamide-bearing solutions were prepared by dissolution of the solid compound (Aldrich, ≥99%) in deoxygenated water. In near-neutral to moderately-acidic solutions, thioacetamide stoichiometrically decomposes to acetic acid (CH_3COOH), ammonia (NH_3) and H_2S with the reaction rate becoming faster upon heating (Pokrovski et al., 2008):

$$CH_3CNH_2S_{(aq)} + 2\ H_2O = CH_3COOH_{(aq)} + NH_{3(aq)} + H_2S_{(aq)} \quad (3)$$

In contrast, acetic acid is kinetically stable at our moderate temperatures (<300 °C) within the run duration, and is known to start significantly decomposing to formic acid and CO_2/CO only above 320–350 °C (Li et al., 2017). Care was taken when preparing HCl-acidified solutions (e.g., Exp6) to avoid early decomposition of thioacetamide and partial H_2S release, by quickly loading the solution and pressurizing the XAS cell within <10 min.

3.3. Experimental and analytical setups

3.3.1. Flexible-cell reactor with rapid sampling (FCR)

The solubility of PtS(s) was measured in aqueous NaHS-NaCl solutions in the temperature range 50–300 °C and the pressure range 100–600 bar (experiment m35, Tables 1 and S1, Fig. S1) using a flexible-cell reactor (FCR) allowing fluid sampling (Coretest®; Rosenbauer et al., 1993). The reactor is equipped with a 100–200 cm^3 flexible inner cell made of gold (99.99% purity) and a rapid-sampling device adapted to S-rich fluids (Kokh et al., 2020). The cell was loaded with the solids (0.15 g PtS, 0.4 g PdS, 2.0 g FeS, 1.8 g FeS_2) and a NaHS solution (1.04 m NaHS + 0.12 m H_2S) under argon atmosphere. The cell was then rapidly compressed to remove the gas phase; the experiment was conducted in the single-phase liquid domain. Multiple fluid extractions (2 to 4) were periodically taken at each temperature step, from 56 °C up to 300 °C and down to 50 °C, at pressures from 100 to 500 bar (depending on the step, see Tables 1 and S1). Injections of water, HCl/NaOH or H_2O_2 concentrated solutions were performed through the sampling line at given steps to modify in situ the sulfur concentration, pH or redox in the experimental fluid. Until step m35/4, when H_2S is a minor species in the fluid and fluid degassing is weak, the solution could directly be sampled with a gas-tight syringe. For the other steps, fluid was sampled under pressure using a rigid titanium vial attached to a pressure valve to avoid any degassing. Sampling procedures using different trap solutions are detailed in Kokh et al. (2017, 2020) and only briefly summarized below.

3.3.2. Analytical methods

At each step of solubility experiment m35 (Tables 1 and S1), multiple fluid samples (usually 3 to 4, 1 to 2 g each) were extracted from the flexible cell. Each sample was destined for a different analysis (see Kokh et al., 2017, 2020 for more details). Sample 1 was aimed to remove the residual solution present in the sampling tube from a previous injection or sampling to avoid cross-

contamination; sample 2 was titrated for reduced sulfur with iodine (I_2) placed in the sampling vial; sample 3 was trapped in ultrapure aqueous 30 wt% NH_3 solution to measure total metal and sulfur contents; sample 4 was trapped in a 1 m zinc acetate ($Zn(CH_3COO)_2$) aqueous solution to precipitate

ZnS (titrated afterwards with I_2, see below) and to measure sulfate (SO_4^{2-}) concentrations in the supernatant. Note that iodine reacts with both sulfide and polysulfide species, while zinc acetate reacts only with sulfide species ($H_2S+HS^-+NaHS^0$) to form the ZnS solid. Vials containing ZnS (sample 4) were acidified with HCl (18 wt%) in the presence of an excess of I_2, which was back-titrated with sodium thiosulfate ($Na_2S_2O_3$, 0.1 mol/L) to determine the total sulfide concentration. Sample 3 was separated into two fractions: one for metal concentration analyses, and the other for total sulfur analyses, after converting all S to sulfate by adding 2 mL of 30 wt% H_2O_2 aqueous solution. The fraction for metal analyses was collected in clean Teflon vials (Savillex®) and processed as followed: i) evaporation of the solution in the vial on a hot plate (70 °C); ii) addition of ~5 mL of aqua regia (1/3 HNO_3, 2/3 HCl) in the closed vial (~120 °C for 3 hours); iii) evaporation of aqua regia on a hot plate until wet residue (70 °C); iv) dilution of the residue with ultra-pure doubly-distilled acids (0.5 wt% HNO_3 plus 1.5 wt% HCl). The use of aqua regia and an HCl-HNO_3 matrix is indispensable to fully solubilize the poorly soluble PtS(s) precipitates and to keep Pt in solution as soluble chloride species $Pt^{II}Cl_4^{2-}$ and/or $Pt^{IV}Cl_6^{2-}$.

Concentrations of Pt and Au in the sampled fluids were measured by inductively coupled plasma - mass spectrometry (ICP-MS) and/or inductively coupled plasma - optical emission spectrometry (ICP-OES). Samples for ICP-MS were further diluted in 2 wt% HNO_3, just before the analytical session, to reduce the Cl^- and SO_4^{2-} ion concentration in solution, which is a source of plasma instability and elevated analytical background in the ICP-MS analysis. The maximum total dissolved load therefore did not exceed 100 ppm in our samples, with S content less than 5 ppm. An ICP-MS Element XR spectrometer was used in our study, enabling detection limits (DL) as low as 1 ppt Pt and quantification limit (QL) of 10 ppt Pt. Two standard solutions (0.19±0.01 and 18.3±0.01 ppb Pt) were used for calibration, and showed excellent signal linearity through zero (R^2_{xy}>0.999). Both ^{194}Pt and ^{195}Pt

isotopes analyzed yielded identical Pt concentrations (within ±2%) demonstrating the absence of spectral interferences. ICP-OES was used to analyze gold and sulfur, which were far more concentrated. Chloride and sulfate ion concentrations were determined by high performance liquid chromatography (HPLC) in water-diluted samples. Sodium ion concentrations were measured using flame atomic absorption spectrometry (FAAS).

3.3.3. X-ray absorption spectroscopy

The X-ray absorption spectroscopy measurements (including both X-ray absorption near edge structure, XANES, and extended X-ray absorption fine structure, EXAFS) at the Pt-L_{III} edge (~11564 eV) were performed at beamline BM30-FAME (Proux et al., 2005) of the European Synchrotron Radiation Facility (ESRF, Grenoble, France). The beamline has an X-ray optics setup with a Si(220) double-crystal monochromator with sagittal focusing for choosing the energy of X-rays delivered from a bending magnet, and two Rh-coated mirrors for harmonic rejection and vertical focusing, yielding a beam spot on the sample of 200×300 μm^2. In transmission mode, silicon diodes collected scattered radiation from a Kapton foil placed in the incidental and transmitted X-ray beam. In fluorescence mode, a Canberra 13-element solid-state germanium detector was placed in the right-angle geometry to the incident beam. The energy position during each scan was monitored in transmission mode using a Pt metal foil whose L_{III}-edge energy was set to 11564.0 eV as the maximum of the spectrum first derivative. Reference solid compounds, PtS(s) and PtS_2(s), were diluted with boron nitride (BN) powder to achieve an above-edge absorbance of one, pressed in 5-mm diameter pellets and recorded in transmission mode at ambient conditions. The experimental solutions were placed in the glassy-carbon inner cell (0.2–0.3 mL volume) of the hydrothermal apparatus, developed at the Néel Institute (Testemale et al., 2005; see also Pokrovski et al., 2006 for details), and were recorded at 250 and 300 °C at 500 bar in fluorescence mode (Table 2). A round-shape cut Pt metal foil (0.4 mm thickness) was placed at the cell

bottom outside the X-ray beam passage to measure, from the amplitude of fluorescence spectra in the fluid, the solubility of PtS(s) that rapidly formed at the metal surface (see section 3.1).

part of the solutions at low Pt concentrations (1–20 ppm Pt), at least 10 to 20 scans of 40 min acquisition time each were necessary. The acquired XAS spectra were analyzed using the Athena and Artemis software (Ravel and Newville, 2005) based on the IFFEFIT program (Newville, 2001) and following previously established protocols (e.g., Pokrovski et al., 2005; Laskar, 2022). Spectra were normalized to the absorption edge height and atomic-background subtracted with a normalization order of 3. Exploitable *k*-ranges were within 3–12 $Å^{-1}$. A Fourier Transform (FT) was applied to extract the frequency-dependent contributions from the backscattering atoms, using a Kaiser-Bessel window with a *dk* value of 3. Fits were performed in *R*-space on both real and imaginary parts of FT to obtain the structural information, such as the interatomic distance (R), the mean square displacement bond length for a given scattering path (so-called Debye-Waller factor, σ^2), and ΔE, which is a non-structural parameter accounting for energy shift between experimental spectrum and FEFF calculations that were used to obtain the amplitude and phase electron scattering factors for backscattering atoms. Fits were performed with *k*-weighting of 1, 2 and 3 to diminish correlations between ($N \times S_0^2$) and σ^2, and R and ΔE, and to improve fit robustness (Ravel and Newville, 2005). The amplitude reduction factor, S_0^2, which is critical for accurate quantification of coordination numbers (N), was set to 0.80 as established on the basis of EXAFS fits of a large number of Pt reference compounds both in fluorescence and transmission modes (Laskar, 2022).

The absorption edge height in transmission mode, which may be used for straightforward determination of dissolved absorber concentrations from XAS spectra (e.g., Pokrovski et al., 2005, 2006), was too small to be quantified for the low Pt concentrations of our experiments. In contrast, the absorption edge height in fluorescence mode is much greater and accurately determined, but required calibrations as a function of detector position as well as matrix absorption corrections to be

converted into metal concentration (e.g., Bazarkina et al., 2014; Pokrovski et al., 2022). Calibrations of the fluorescence signal were performed using three solutions of $K_2PtCl_{4(aq)}$ of ~1, 10 and 100 ppm Pt, in which NaCl was added to adjust the matrix absorbance to make it similar to that of the experimental

solutions. The calibrations were made as a function of detector and sample positions, because these positions were varied during the different experiments to optimize the fluorescence signal depending on the Pt concentration (see Appendix A for more details). The Pt concentration m_X in each scan (*X*) is determined as:

$$m_X = m_{STD} \times \frac{\Delta\mu_X}{\Delta\mu_{STD}} \quad (4)$$

where m_X and m_{STD} are, respectively, the Pt experimental and standard concentrations(in mol/L), and $\Delta\mu_X$ and $\Delta\mu_{STD}$ are, respectively, the absorption edge height of the sample and the absorption edge height of the standard corrected to the same absorbance and position as the experimental sample. Volumetric concentrations were converted to molality using the fluid density at the experimental *T-P* conditions assuming that density is equal to that of aqueous NaCl solution of the same solute weight concentration (Pokrovski et al., 2009). The combined uncertainty on Pt concentration determination is 5 to 30 % of the total value, depending on the experiment (Table 2).

3.4. Thermodynamic modeling

Equilibrium thermodynamics calculations were performed to quantify the chemical speciation and the solubility controlling parameters (pH, f_{O_2}, activity of sulfur ligands) in the fluid phase both to optimize the choice of experimental solution compositions and to derive Pt species stoichiometry and stability constants. The sources of thermodynamic data used in these calculations are reported in Table S2. Data for major aqueous species were taken from the updated version of the Supcrt92 database (Johnson et al., 1992; Zimmer et al., 2016), based on the revised and extended Helgeson-Kirkham-

Flowers model (HKF; Tanger and Helgeson, 1988; Oelkers et al., 2009; Sverjensky, 2019). More recent data were taken for polysulfide dianions (S_n^{2-}, $2 \leq n \leq 8$; Barré et al., 2017), S_3^- radical ion (Pokrovski and Dubessy, 2015), and HCl^0 (Tagirov et al., 1997). The thermodynamic properties of PtS(s) were taken

from Sassani and Shock (1998), whose original sources are detailed in Table S3. These data were preferred to the more recent theoretical estimations of Karzhavin (2007), who based his analysis on inter-element correlations which may be subjected to significant uncertainties. The properties of aqueous volatile non-electrolyte species (H_2S, SO_2, H_2, and O_2) were adopted according to the equation of state of Akinfiev and Diamond (2003), which performs better than HKF for moderate pressures (< 1–2 kbar). The $NaHS^0$ ion pair, which represent a significant fraction of reduced sulfur at pH≥7, was also included assuming that its dissociation constant is equal to that of $NaCl^0$ at all *T-P*. The standard state of solid phases and H_2O is unit activity at all temperatures and pressures; the standard state of aqueous species is 1 molal aqueous solution whose behavior is ideal. The HCh software (Shvarov, 2008) was used for thermodynamic calculations. The module OptimA connected to HCh (Shvarov, 2015) was used to choose among possible Pt-HS species ($Pt^{II}(HS)_2^0$, $Pt^{II}(HS)_3^-$, $Pt^{II}(HS)_4^{2-}$) inferred from the EXAFS and MD data (see below), based on the statistically best match of the experimental solubility data points. Then, the standard Gibbs energy value of the chosen complex was optimized by regression of the experimental data points of Pt solubility obtained at a given *T-P* condition, while taking into account the data point relative weights (equal to $1/\sigma$, where σ is the standard deviation of solubility value in $\log_{10}$ units). The overall errors on the resulting constants of solubility reactions of PtS(s) with formation of Pt-HS complexes (see below), which stem from the experimental data point scatter and the uncertainties in the thermodynamic properties, are typically less than ±0.5 $\log_{10}$ units (see Pokrovski et al., 2015, 2021 for a more detailed assessment of errors related to the choice of thermodynamic data).

3.5. Thermodynamic analysis of experimental data from the literature

To provide more thermodynamically consistent comparisons between the stability constants of Pt-HS complexes derived in this study and previous work, the same thermodynamic data frame must be used. This is because the interpretation of PtS(s) solubility data in terms of the dominant Pt-HS

complexes as a function of pH, redox and sulfide ligand activity is strongly dependent on the exact values of those parameters, which are in turn calculated using thermodynamic data sources that were different in different studies. Therefore, we attempted to reanalyze the large set of PtS(s) solubility data acquired in the seminal work of Gammons and Bloom (1993) using our thermodynamic database (Table S2) and more robust thermodynamic analysis tools (OptimA) which were not available at the time of their original work. These authors studied PtS(s) solubility between 200 and 300 °C at P_{sat} in NaHS-NaOH-HCl aqueous solutions with sulfide concentrations of 0.4–1.0 m in the pH range 6.4–8.4. These conditions are very similar to those of our study. The set of solubility measurements at each temperature (16, 13 and 14 data points at 200, 250, and 300 °C, respectively, Table A5 in Gammons and Bloom, 1993) has been processed using the thermodynamic software OptimA coupled with HCh to analyze the data in terms of Pt-HS species stoichiometry found in our experiments (in particular $Pt(HS)_4^{2-}$, see section 4) and to derive their stability constants. In these calculations, we also took into account the amount of H_2S in the vapor phase, which made between 20 and 30 % of the total experimental tube volume (from our communication with C. Gammons).

No attempt was made to re-process in a similar way the data of Pan and Wood (1994) and Filimonova et al. (2021) because their speciation is likely to be different from ours. Filimonova et al. (2021) used much more dilute H_2S solutions (<0.1 m) in which lower-ligation number complexes are likely to be dominant (e.g., $Pt(HS)_2^0$). Pan and Wood (1994) employed sulfate-sulfide solutions in which Pt complexes with the trisulfur ion or polysulfide dianions might form in addition to Pt-HS species. Furthermore, we have identified errors in the reported stability constants for some of the suggested Pt-HS species in their study (e.g., for $Pt(HS)_3^-$ and $Pt(HS)_4^{2-}$ in their Table 4). Therefore, to allow formal comparisons with other data sources, we just manually recalculated Pan and Wood's (1994) values for

these complexes using the reported Pt solubility, H_2S activities and pH (from their Table 3). The re-processed or re-calculated values from these previous studies are reported in Table 5 and will be compared with our results in section 5.

3.6. First principles molecular dynamics simulations

First principles molecular dynamics (FPMD) simulations (Car and Parrinello, 1985) were performed using the simulation code CP2K (Kühne et al., 2020), within the Born-Oppenheimer framework. The molecular dynamics (MD) simulations were run in the *NVT* ensemble (constant number of particles *N*, volume *V*, and temperature *T*), using a velocity-Verlet integrator (with a time step Δt = 0.5 fs) and a canonical sampling/velocity rescaling (CSVR) thermostat (Bussi et al., 2007; with τ_{CSVR} = 1 ps). A cutoff of 800 Ry was used for the electronic density and dispersive interaction corrections were added using the DFT-D3 scheme with a cutoff radius of 15 Å (Grimme, 2006). A *molopt* double-zeta valence plus polarization (DZVP-MOLOPT) basis set was used for FPMD calculations (VandeVondele and Hutter, 2007), with the Gœdecker-Teter-Hutter pseudo-potential (Gœdecker et al., 1996; Hartwigsen et al., 1998; Krack, 2005). The PBE exchange-correlation functional (Perdew-Burke-Ernzerhof; Perdew et al., 1996; Perdew and Levy, 1997) was used because it usually yields good results for heavy transition metals such as Pt (Vícha et al., 2015). The interatomic distances of the complexes were initially optimized by static density functional theory (DFT), using the Orca program (Neese, 2012, 2018) and with PBE0 exchange-correlation functional (Adamo and Barone, 1999). Scalar relativistic effects have been included within the zeroth order regular approximation (ZORA) to the Dirac equation and an all electron TZVPP basis set was used.

The first principles thermodynamic integration method (Resat and Mezei, 1993; Sprik and Ciccotti, 1998; Bühl et al., 2006, 2008) was adapted to estimate the energetics of complexation reactions between the Pt^{2+} ion and HS^- ligands. The approach consists in constraining the bond length

between the central Pt ion and the S atom of one of the surrounding HS^- ligands, to determine the force needed for the system to keep this Pt-S distance at the constrained length. The force is derived by a Lagrange multiplier (Sprik and Ciccotti, 1998) when pulling apart the Pt and S atoms from a first

coordination shell distance between Pt and HS (~2.3 Å), up to a much longer distance at which Pt and the ligand virtually stop interacting with one another (>5–6 Å). Then the time-averaged forces calculated at each Pt-S distance were integrated along the distance path, to obtain the corresponding Pt-S bond free-energy as a function of Pt-S distance. Different Pt-S bond distances were chosen to minimize the number of runs while keeping a good precision in the force integration, with differences between successive bond lengths from 0.05 to 0.5 Å depending on the force variations with the Pt-S distance. The stepwise reaction constants corresponding to the formation of a Pt-S bond was then derived as detailed in Appendix A. Notably, the Pt-S bond was modeled as a spring (Ramachandran et al., 2008) yielding stepwise reaction constants independent of the accessible volume for the free species in the simulation box.

We used a box of 128 water molecules and one complex among the different Pt-HS complexes (Fig. 2). This configuration corresponds to a sulfur concentration of 0.5 to 2 m, similar to that in our experiments, even though these values are not directly comparable because of the periodic boundary conditions used in the simulation. The size of the cubic box (17×17×17 Å, Table 3) was kept the same for all runs, so that the water density surrounding the complex would be unchanged, with pressure values in the range of 500–700 bar. The box contained no counter ions in order to accelerate the simulations and to have all HS^- ions bounded to Pt. The influence of the presence of 2 additional Na^+ cations in the simulation box was tested, with the Pt-S bond length fixed at 2.80 Å for a run with the job 4 configuration (Table 3), and yielded the same within errors force value as without Na^+. In the absence of counter ions, the simulation box was electrically neutralized by a uniformly charged background (–1, 0, +1, and +2 for jobs 1, 2, 3, and 4, respectively). This procedure did not influence the force determination in our case in the absence of redox reactions that would have otherwise required

charge transfer. Note that the number of water molecules in our simulations is much greater than in previous studies ($N(H_2O)$=128 vs $N(H_2O)$=55; Mei et al., 2015a, for example). The greater number of H_2O molecules prevents the complex to artefactually interact with its periodic replica, being

surrounded by nearly two water solvation shells. The step was set to 0.5 fs, for a whole simulation duration of 5 to 7 ps. The first 700 steps (0.35 ps) were not used in the force determination to allow for the chemical bonds to equilibrate with the newly constrained Pt-S distance.

4. RESULTS

4.1. X-ray absorption spectroscopy

4.1.1. XANES analysis

Normalized Pt L_{III}-edge XANES spectra of sulfur-bearing aqueous solutions (0.9–2.4 m H_2S/HS^-) from three Pt XAS experiments (Exp6, 7 and 9) at 300 °C/500 bar and one experiment (Exp3) at 250 °C/500 bar are plotted in Fig. 3a and compared with spectra of the $Pt^{II}S$ and $Pt^{IV}S_2$ solid reference compounds. It can be seen that both the amplitude and the energy position of the white-line (summit at 11567.5 eV) of the spectra of dissolved Pt are very similar to that of PtS(s) in which the metal is in a formal oxidation state of II and coordinated by 4 sulfur atoms in a square-planar geometry. Such coordination geometries are typical of most Pt^{II} organic and inorganic compounds (Cotton et al., 1988) that contain same or different ligands (e.g., HS^- and H_2O/OH^-). In the absence of reference XAS spectra for such compounds, we attempted to discriminate among the most plausible Pt-HS complexes ($Pt^{II}(HS)_2(H_2O)_2^0$, $Pt^{II}(HS)_3(H_2O)^-$, and $Pt^{II}(HS)_4^{2-}$) by calculating their theoretical XANES spectra. These calculations used the finite difference method near edge structure (FDMNES) package (Joly, 2001; Bunău and Joly, 2009) with complexes geometry generated by static DFT calculations (Fig. 2). Details of FDMNES calculations may be found in Pokrovski et al. (2021, 2022). XANES spectra calculated using the well-known crystallographic structures of the Pt reference solids ($Pt^{II}S$, native Pt and $K_2Pt^{II}Cl_4$) are

very close to those of the experimental spectra (Fig. S8), correctly reproducing both the while line position and amplitude and the energy position of the post-edge resonances in XANES spectra. XANES spectra calculated from DFT-generated geometries of aqueous complexes are also close to those of

averaged configurations from FPMD snapshots (Pokrovski et al., 2022). It can be seen in Fig. 3b that our experimental XANES spectrum (represented by Exp3) is very different in white-line amplitude, post-edge shape and energy positions from the simulated XANES spectrum of $Pt(HS)_2(H_2O)_2^0$. The experimental spectrum is much closer to the calculated spectra of $Pt(HS)_3(H_2O)^-$ and $Pt(HS)_4^{2-}$. The FDMNES-calculated spectrum of $Pt(HS)_4^{2-}$matches slightly better than that of $Pt(HS)_3(H_2O)^-$ the post-edge spectral pattern and amplitude of the experimental spectrum, even though the differences remain rather small. Thus, the most likely species in our experimental solutions is either trihydrosulfide or tetrahydrosulfide or a mixture of both. EXAFS spectra provide additional constraints on the stoichiometry of Pt sulfide complexes as shown below.

4.1.2. EXAFS analysis

Acquiring EXAFS spectra from high *T-P* hydrothermal fluids at ppm-level absorber concentrations is challenging. Only one experiment (Exp3) yielded high-quality EXAFS exploitable to 11.5 $Å^{-1}$ after summing up at least 20 scans × 40 min acquisition time per scan (Fig. 4), allowing us to perform statistically robust EXAFS fits with a number of variables significantly smaller than the number of independent points (see Ravel and Newville, 2005; Kelly et al., 2008). The EXAFS derived Pt-S distance is 2.30±0.01 Å (Table 4 and Fig. 4), which is identical within errors to the crystallographic Pt^{II}-S distance of 2.31 Å in PtS(s). This distance is shorter than that of mixed Pt^{II} and Pt^{IV} complexes with HS^- and S_3^- ligands in sulfide-sulfate solutions as derived from EXAFS in a recent study, Pt-S = 2.32 to 2.36 Å (Pokrovski et al., 2021). This difference thus indirectly suggests the absence in our system of polysulfide complexes that are expected to have longer Pt-S distances. The fitted mean square

displacement bond length (σ^2~0.003 Å²) of the EXAFS spectrum from this experiment is within the range of values found for linear/planar-square (Au/Pt)-($HS^-/S_3^-/Cl^-$) complexes in recent XAS studies (σ^2 ranging from 0.001 to 0.006 Å²; Pokrovski et al., 2009, 2015, 2021; Tagirov et al., 2019). The average

number of sulfur atoms in the nearest Pt coordination shell is 4.0±0.5, suggesting that $Pt(HS)_4^{2-}$ is likely the dominant complex in the experimental solution, which is also in agreement with the XANES qualitative observations above. The predominance of $Pt(HS)_4^{2-}$would also be supported by the presence of a multiple scattering contribution at 4.6 Å, which is double the Pt-S distance of 2.3 Å (Fig. 4, Table 4) and arises from the first Pt coordination shell, thereby pointing to a symmetrical square-planar geometry. However, given the intrinsically high uncertainties (typically 10 to 20 %) on the determination of coordination numbers from EXAFS fits, the presence of oxygens arising from the coordinating H_2O molecules in the complex (Fig. 2) cannot be fully excluded. Note that O, being lighter than S, is therefore a much weaker EXAFS backscatter; as a result, the EXAFS signal is dominated by sulfur atoms. In an attempt to detect O in the EXAFS signal, we applied a statistical analysis developed in Kelly et al. (2008) and used in Bazarkina et al. (2010) for analogous $[Pd(H_2O)_nCl_{4-n}]$ complexes. This analysis is based on the comparisons of the reduced (χ^2_{red}) factors between EXAFS fits performed either with S atoms exclusively or with both S and O atoms in the first Pt shell. We found that the addition of oxygen in the first shell yields N_O values up to 0.5 atoms but does not improve the EXAFS fit quality in a statistically significant manner (e.g., χ^2_{red}~25 for the model with S and O atoms is not significantly different from that for the model with S atoms only, χ^2_{red}~33; Table 4). Supported by the XANES results above, these findings suggest that $Pt(HS)_4^{2-}$ is the dominant complex in our experiments at 250–300 °C and 1–2 m sulfide concentration. Further support to this stoichiometry is provided by FPMD results as shown below.

4.2. Results from molecular dynamics

The FPMD simulations of Pt-HS complexes were performed at 300 °C and 500–700 bar, with different starting geometries generated by static DFT calculations ($Pt^{II}(HS)(H_2O)_3^+$, $Pt^{II}(HS)_2(H_2O)_2^0$, $Pt^{II}(HS)_3(H_2O)^-$ and $Pt^{II}(HS)_4^{2-}$; Fig. 2 and Table 3). The geometry of these square-planar complexes

remained stable over the whole MD simulation duration (~5–7 ps). The mean Pt-S distance from FPMD is 2.38±0.01 Å for the $Pt(HS)_4^{2-}$ complex (Table S4), which is longer than the EXAFS-derived experimental value (2.30±0.01 Å) for the experimental solution at 250 °C (Table 4). Note that compared to XAS measurements, similarly longer (by 0.04 to 0.1 Å, Table S4) metal-ligand distances are systematically predicted by FPMD (e.g., Spezia et al. 2008, 2012; Mei et al., 2015a; Pokrovski et al., 2022). The mean Pt-S distance from DFT for the $Pt(HS)_4^{2-}$ complex (2.35 Å) is closer to XAS measurements, which was attributed to the use of a pseudopotential in FPMD that only approximates the effect of core electrons, whereas static DFT methods treat both core and valence electrons explicitly (Pokrovski et al., 2022). The Pt-S mean bond lengths from FPMD were 2.37±0.01 Å, 2.37±0.01 Å and 2.28±0.01 Å, for $Pt(HS)_3^-$, $Pt(HS)_2^0$ and $Pt(HS)^+$, respectively (Table S4). The generally slightly shorter Pt-S bond lengths for complexes with lower numbers of HS^- ligands are likely due to the presence of water, with shorter Pt-O distances of 2.10–2.29±0.03 Å (Table S4), leading to an overall contraction of the Pt coordination shell.

The stepwise reaction constants for the four potential Pt-HS complexes calculated using the FPMD force integration method, as detailed in Appendix A, are reported in Table S5 for the reaction:

$$Pt(HS)_{x-1}^{3-x} + HS^- = Pt(HS)_x^{2-x},\ 1 \le x \le 4 \quad (5)$$

These may be converted, for practical purposes, to cumulative reaction constants β_n, describing the solubility of PtS(s) in terms of the three most plausible hydrosulfide complexes:

$$PtS_{(s)} + 3\ H_2S_{(aq)} = Pt(HS)_4^{2-} + 2\ H^+ \qquad \log_{10}\beta_4 \quad (6)$$

$$PtS_{(s)} + 2\ H_2S_{(aq)} = Pt(HS)_3^- + H^+ \qquad \log_{10}\beta_3 \quad (7)$$

$$PtS_{(s)} + H_2S_{(aq)} = Pt(HS)_2^0 \qquad \log_{10}\beta_2 \quad (8)$$

This conversion requires a value of the reaction constant for the Pt^{2+} ion:

$$Pt^{2+} + H_2S_{(aq)} = PtS_{(s)} + 2\ H^+ \quad (9)$$

This value was adopted based on the data of Sassani and Shock (1998) for the Pt^{2+} thermodynamic properties in the framework of the HKF model, which are also consistent with the choice of other thermodynamic data in this study (Table S2). Sassani and Shock's (1998) set of data was preferred to an alternative Pt^{2+} thermodynamic set reported by Tagirov et al. (2015). The latter may be subjected to potentially large uncertainties related to the extrapolation to infinite dilution of the low-temperature values of the formation constants of $PtCl_n$ ($1 \le n \le 4$) species from Pt^{2+} (Elding, 1972a,b, 1978) on which the Pt^{2+} thermodynamic properties at high temperatures are currently based.

4.3. Results of solubility experiments from flexible-cell reactor (FCR) and in situ XAS

4.3.1. PtS(s) solubility under reducing conditions from FCR experiments

In experiment m35 conducted in FCR at each corresponding step, reduced sulfur concentrations analyzed with iodine and zinc acetate are similar (Table S1), demonstrating that reduced sulfur species other than sulfide are negligible. The total sulfur concentration (S_{tot}) is also similar to the sulfide concentration within their analytical errors (±10% each). Sodium and chloride concentrations have smaller analytical errors and remain stable during a given step (within ±5%). These values therefore were used to more accurately determine dilution factors from the injections and the resulting fluid composition. Dissolved gold concentrations stabilize within <2 days during each step following an injection, suggesting that both pH and f_{O_2} that control Au(s) solubility equilibrate equally rapidly. The experimental Au concentrations are within <0.5 log unit of the predicted concentrations of the $Au(HS)_2^-$ complex using the available thermodynamic data sources (Table S2). Platinum concentrations in experiment m35 vary in the range $(0.1–14)\times10^{-6}$ m Pt (Tables 1 and S3, Fig. S1). They exhibit systematic changes with temperature (50–300 °C), pH (5.0–7.8) and sulfide concentration (0.5–

1.2 m). A steady state is usually attained after a few days following the temperature change or the modification of the fluid composition via injection, suggesting that fluid equilibrium is likely to be reached with PtS(s). With the increase in temperature from 200 to 300 °C, at a constant sulfur concentration and in the pH range 6.8–7.5, the Pt concentrations remained similar (3–4×10^{-6} m). At 300 °C, the decrease of pH by one unit (from 6.8 to 5.7) results in a Pt concentration decrease of about one log unit, whereas the sulfide concentration only slightly decreased (from 1.0 to 0.8 m). The PtS(s) solubility values at a given temperature quickly respond to the changes in pH upon HCl injection. The pH dependence is consistent with the formation of electrically charged Pt-HS complexes, most likely $Pt(HS)_4^{2-}$ (equation 6). The Pt concentration variations with pH at lower temperatures (50–250 °C) are more difficult to interpret without in-depth thermodynamic analysis, as the sulfide concentrations also changed by a factor of two between the alkaline and acidic experimental steps at the same temperature. The influence of pressure on PtS(s) solubility was found to be negligible within the analytical errors, at least from 200 to 600 bar, which is consistent with the low compressibility of aqueous solutions at moderate temperatures (50–300 °C).

4.3.2. PtS(s) solubility from XAS experiments

In the XAS experiments, the measured Pt concentrations range from 6×10^{-6} to 60×10^{-6} m, for reduced sulfur concentrations of 0.9–2.4 m and pH of 5–10 (Table 2). In situ XAS measurements offer the possibility to monitor the temporal evolution of dissolved concentrations far more accurately than hydrothermal batch reactor experiments. Changes in the amplitude of absorption edge height of fluorescence spectra $\Delta\mu_{Pt}$ *(fl)*, proportional to Pt concentration, were observed with time at a given *T*-*P* (Fig. S3). In the experiments with NaHS aqueous solutions, Pt concentrations slightly increased (<10 % of the value) before attaining a steady state after a few hours of dissolution reaction. In the experiments with thioacetamide, Pt concentrations either decreased to stable values at 250 °C after

10 h, or increased to relatively stable values at 300 °C after 3–5 h (Fig. S3). Such different dissolution patterns may be due to combined kinetics of thioacetamide decomposition (reaction 2) and PtS(s)-fluid equilibration. Therefore, in the further thermodynamic analysis, we used Pt solubility data

measured after 4 hours in each XAS experiment (except Exp3 at 250 °C for which a 10 h steady state was adopted). These data were assumed to correspond to equilibrium. Note that the obtained results for experiments with NaHS are very similar to the FCR solubility experiment, supporting the validity of Pt concentration determination from in situ XAS data. For example, XAS experiment Exp7 at 300 °C and 500 bar with S_{red}=0.97 m and pH=8.3 yielded (6.5±0.5)×10^{-6} m Pt at steady state, which is similar within errors to the value of (4±2)×10^{-6} m from the much longer FCR experimental step with S_{red}=1.12 m and pH=6.8. All XAS experiments, but Exp9 (see below), were used, together with the FCR experiment, to derive the stability constants of $Pt(HS)_4^{2-}$ (see next section). The only exception is the most alkaline pH experiment (Exp9; pH=10), which yielded too high Pt solubility and the resulting $\log_{10}\beta_4$ constant (Table 2, Fig. S2), compared to all other experiments conducted at pH <9. This discrepancy might be due to the formation of additional Pt-HS-S complexes at such alkaline pH (e.g., Filimonova et al., 2021), probably with the S^{2-} ion that was predicted to form in significant amounts at pH >10 according to theoretical estimations of its dissociation constant by Phillips and Phillips (2000). However, more direct experimental data on sulfur speciation at such alkaline pH at elevated temperatures are required before the S^{2-} ion could be considered in speciation models. Therefore, we omitted this alkaline experiment from further discussions.

4.3.3. PtS(s) solubility at oxidizing conditions in FCR

In step m35/14 at 50 °C and 260 bar of the FCR experiment, hydrogen peroxide was injected to investigate the effect of partial sulfur oxidation on PtS(s) solubility. Both S_{tot} and S_{red} analyzed concentrations (H_2S+HS^-+$NaHS^0$ = 0.13–0.16 m, Table S1) are much lower than the expected S_{tot} of 0.32

m according to the mass balance calculations of the remaining and injected fluid amounts, while analyzed sulfate concentrations were below 0.01 m (Table S1). Thermodynamic calculations predict the precipitation of native sulfur, in agreement with these analyses and an increase of f_{O_2} by 15 log

units (Table 1). Platinum concentrations in the fluid were 1 to 2 orders of magnitude higher compared to the predicted Pt concentrations assuming $Pt(HS)_4^{2-}$. The findings of this single exploratory measurement would therefore suggest the formation of additional complexes, most likely with polysulfide ions produced via H_2S oxidation that may be strong ligands for Pt (e.g., Pokrovski et al., 2021). According to our thermodynamic calculations of the fluid speciation, among them, S_5^{2-} would be the most abundant one, reaching concentrations of 5×10^{-4} m at these *T*-*P* conditions (note that the radical S_3^- ion is rather minor at such low temperatures, $[S_3^-]<10^{-6}$ m). Even though the quantitative complexation capacity of S_5^{2-} for Pt is unknown, complexes such that $Pt^{II}(S_5)_2^{2-}$ and $Pt^{IV}(S_5)_3^{2-}$ existing in solids (Wickenden and Krause, 1969; Laskar, 2022) may equally form in aqueous solution. This solubility step was therefore ignored in the derivation of Pt-HS complexes stability constants that follows.

4.4. Derivation $Pt(HS)_4^{2-}$ stability constants

The FPMD-derived stepwise complexation constant of the formation of $Pt(HS)_4^{2-}$ from $Pt(HS)_3^-$ ($\log_{10}K_4$ = 6.8±1.0, reaction 4, Table 3), implies that the tetrahydrosulfide dominates over trihydrosulfide in solution at HS^- concentrations above 10^{-7} m at 300 °C and slightly acidic to alkaline pH. These fluid parameters cover most natural and experimental fluid compositions examined here and in previous work. The Pt dihydrosulfide complex would have concentrations at least 4 orders of magnitude lower than trihydrosulfide at such conditions ($\log_{10}K_3$ = 10.5±0.9). The absolute concentrations of the three complexes calculated in equilibrium with PtS(s) for our range of sulfide concentrations (0.8–2.4 m) at 300 °C and 500 bar are compared with experimentally measured values

in Fig. 5. It can be seen that $Pt(HS)_4^{2-}$ concentrations are only slightly lower (<0.5 log unit) than in most experiments, whereas the predicted concentrations of $Pt(HS)_2^0$ and $Pt(HS)_3^-$ using our MD constants are negligibly small. Even though MD-derived stability constants are subjected to significant uncertainties (see Appendix A for more details), when combined with the independent in situ XANES and EXAFS results, they strongly support the conclusion that $Pt(HS)_4^{2-}$ would be the dominant species at our conditions.

These constraints on the complex stoichiometry enable derivation of the stability constants of $Pt(HS)_4^{2-}$ from PtS(s) solubility data obtained in FCR and XAS experiments in this study. In this derivation, the standard molal Gibbs energy of the complex ($G^0_{T,P}$) was determined by fitting the solubility data at each experimental temperature and pressure using the OptimA software (Fig. S2). The differences between experimental and regressed solubility data points at 50, 100, 200, 250, and 300 °C do not exceed 1 log unit, which may be considered as a decent agreement in light of the ppb-level measured absolute Pt concentrations. Furthermore, the FCR and XAS data are in fairly good agreement, the differences between them being within 0.5 log unit (Figs. 5 and S1). The obtained values were converted to the reaction constant (Table 5) using the Gibbs energies of the other reaction constituents from thermodynamic data sources in Table S2. Note that the solubility-derived value at 300 °C and 500 bar is within 1 log unit of the independent MD-predicted value, which was not used in the regression. The solubility-derived $\log_{10}\beta_4$ values generated in this study (Fig. 6, blue diamonds) were fitted by a linear function of the reciprocal of absolute temperature:

$$\log_{10}\beta_4 = 0.9\times1000/T(K) - 19.7\ (\pm0.5) \quad (10)$$

5. DISCUSSION

5.1. Structure and stoichiometry of Pt-HS complexes in hydrothermal fluids

Our direct spectroscopic data coupled with molecular dynamics calculations demonstrate that the square-planar platinum tetrahydrosulfide $Pt(HS)_4^{2-}$ is likely the most stable Pt^{II} complex in sulfide-rich hydrothermal fluids, at least at moderate temperatures (<350 °C). Its structure and stoichiometry

are typical of most inorganic Pt^{II} complexes known in chemistry (e.g., Cotton et al., 1988). Furthermore, similar stoichiometries and structures were found in model hydrothermal fluids for $Pt^{II}Cl_4^{2-}$, which may be the major Pt chloride complex in saline sulfur-free hydrothermal-magmatic fluids (Tagirov et al., 2019), as well as for the analogous $Pd^{II}(HS)_4^{2-}$ predicted using FPMD to be the most stable among Pd^{II}-HS complexes (Mei et al., 2015a), and for $Pd^{II}Cl_4^{2-}$ shown to be stable in highly saline S-free solutions at moderate temperatures (Bazarkina et al., 2013; Tagirov et al., 2014). The formation of doubly charged chalcophile metal complexes, coordinated with S ligands was also demonstrated for $Mo^{VI}S_4^{2-}$ (Liu et al., 2020), and $Pt^{II}(HS)_2(S_3)_2^{2-}$ and $Pt^{IV}(HS)_3(S_3)_2^{2-}$ (Pokrovski et al., 2021). The stability of such complexes, at least at temperatures below 350 °C in liquid-like density fluids, is in line both with the high chemical affinity of the metal for reduced sulfur and with the relatively high dielectric constant of aqueous solution at such temperatures (>10) stabilizing negatively charged species (e.g., Brimhall and Crerar, 1987).

Our direct structural results place additional constraints on the interpretation of the available literature solubility data in terms of complex stoichiometry. Such data are intrinsically difficult to interpret based exclusively on the bulk solubility data as a function of estimated fluid parameters such as pH and HS^- concentration, usually varying only in a narrow range in experimental studies. These limitations may explain the apparent disagreement of our findings with the available bulk solubility measurements of PtS(s) at conditions very similar to those of our study. For example, $Pt(HS)_2^0$ and $Pt(HS)_3^-$ were suggested as the dominant species by Gammons and Bloom (1993), but the large scatter intrinsic to the solubility-pH and solubility-$a(HS^-)$ dependences in their study renders such stoichiometries uncertain. Similarly, Pan and Wood (1994) failed to derive a definite Pt complex

stoichiometry from their solubility measurements and therefore reported a long list of alternative complexes, from $Pt(HS)^+$ to $Pt(HS)_4^{2-}$, at temperatures <350 °C and sulfide concentrations of >0.1 m.

$Pt(HS)_4^{2-}$ would become less stable and over dominated by lower ligation number complexes. This tendency would be in agreement with the decrease of both fluid density and dielectric constant favoring ion association and uncharged or weakly-charged species stability (Tödheide, 1982; Walther and Schott, 1988; Da Silva et al., 2009; Hou et al., 2020). For Pt, such a tendency was likely to be confirmed by Kokh et al. (2017) and Filimonova et al. (2021) who inferred, from bulk solubility measurements, $Pt(HS)_2^0$ to be the dominant Pt species in much more dilute H_2S solutions (≤0.05 m) and temperatures of 450 °C. In addition, ion-pairing with alkali ions may contribute to the metal speciation at such conditions as shown by solubility studies (e.g., Zajacz, 2010, 2011). Independently, Mei et al. (2014) predicted, using MD simulations, the increasing formation of ion pairs between highly charged complexes and alkali counter-ions (Na^+, K^+) with decreasing the fluid density below 0.7 g/cm^3 (e.g., $NaCuCl_2^0$ formed at the expense of $CuCl_2^-$). The general tendency for lowering electric charge and ligation number of Pt and other metal complexes with increasing temperature is also supported by recent experiments performed in S-free magmatic brines (800–1000 °C, 2 kbar; Sullivan et al., 2022b), indicating the predominance of $PtCl_2^0$ and $PtCl_3^-$ complexes rather than $PtCl_4^{2-}$. Similar complexes for Pd, $PdCl_2^0$ and $PdCl_3^-$, were also found at such conditions (Sullivan et al., 2022a).

5.2. Equilibrium constants of Pt-HS complexes and solubility of PtS(s)

The equilibrium constants of PtS(s) dissolution reactions as Pt-HS complexes from this and previous studies are summarized in Table 5 and the solubility of PtS(s) calculated using these data is shown in Fig. 5. Our β_4 constants for $Pt(HS)_4^{2-}$ are higher than the only directly reported values of Gammons and Bloom (1993) in whose speciation model the tetrahydrosulfide complex was judged to

be subordinate compared to the supposedly dominant Pt di- and trihydrosulfide species (see the section above). We, therefore, re-analyzed their solubility data in terms of $Pt(HS)_4^{2-}$ using the OptimA software. The resulting re-calculated average constants β_4 are in agreement with our values within 1–2 log units over the *T* range 200–300 °C (Table 5), despite, as the authors recognized themselves, the assignment of stoichiometries from their experimental points was prone to considerable error. Their study yields PtS(s) solubilities within ±1 log unit of our values in the *T* range 200–300 °C at S concentrations of 0.1 to 1 m at near-neutral pH of 5–8 (e.g., Fig. 6). Similarly, we re-calculated $\log_{10}\beta_4$ values from the PtS(s) solubility experiments of Pan and Wood (1993) in more oxidizing sulfate-sulfide solutions in the *T* range 200–300 °C, and obtained $\log_{10}\beta_4$ giving values within 0.4 to 2.3 log units of our values (Fig. 6 and Table 5). The concentrations of intermediate-valence S species, such as S_3^-, which has a very strong affinity for Pt (e.g., Pokrovski et al., 2021), are rather small ($S_3^-/H_2S < 10^{-3}$), as we estimated in Pan and Wood's (1994) experimental solutions of using the thermodynamic properties of S_3^- (Pokrovski and Dubessy, 2015). Thus, the Pt speciation model with $Pt(HS)_4^{2-}$ as the main complex as supported by our MD, XAS, and solubility data, offers more coherence between Gammons and Bloom's (1993) and Pan and Wood's (1994) studies, with a difference between $\log_{10}\beta_4$ values from these studies being within only 1 log unit in the 200–300 °C range (Fig. 6 and Table 5). By contrast, the crying discrepancy of the $Pt(HS)_2^0$ β_2 values, between our MD estimations and both solubility studies, with differences up to 18 log units at 300 °C (Table 5), strongly suggests that $Pt(HS)_2^0$-based models are inadequate, at least at moderate temperatures. Thus, first principles free energy calculations provide important independent constrains on speciation models.

6. GEOCHEMICAL SIGNIFICANCE OF PLATINUM HYDROSULFIDE COMPLEXES IN HYDROTHERMAL FLUIDS AND COMPARISON WITH GOLD

The stability constants of $Pt(HS)_4^{2-}$ generated in this study allow for improved predictions of Pt transport in moderate-temperature hydrothermal fluids. Figure 7a shows PtS(s) solubility in a typical saline fluid (10 wt% NaCl equivalent) under redox conditions corresponding to those of the

conventional Ni-NiO mineral oxygen buffer (NNO), as a function of pH and S content from 0.01 to 1 m, at 300 °C and 500 bar. It can be seen that the solubility is dominated by $Pt(HS)_4^{2-}$ at acidic to alkaline pH, whereas the contribution of $PtCl_4^{2-}$ is restricted to very acidic (pH<3) and sulfur-poor (<0.01 m) fluids. Note that the contribution of hydroxide and sulfate complexes (not shown here) is much smaller, less than 1 Pt atom per kg of fluid, according to the available thermodynamic predictions of Sassani and Shock (1998). The absolute PtS(s) solubility is negligibly low at acidic conditions (<1 ppt Pt). The maximum solubility is attained at near-neutral pH (6–7) as $Pt(HS)_4^{2-}$. However, the total Pt dissolved concentrations remain too small (e.g., <0.1 ppb Pt at 0.1 m S and pH 5) to account for significant Pt transport in most epithermal environments. For example, such Pt dissolved concentrations would have required $>10^{11}$ cubic meters of fluid to form a modest deposit of 10 tons of Pt, providing an extremely focused fluid flow and 100% precipitation efficiency. Such fluid amount is equivalent to the global flux of water through all terrestrial subduction zones for 1000 years (e.g., Wallace, 2005), and therefore would be geologically implausible. Therefore, it is unlikely that both Pt-Cl and Pt-HS may explain the multiple instances of PGE remobilization and concentration commonly observed in hydrothermal environments (Hanley, 2005; Mungall and Naldrett, 2008; Economou-Eliopoulos, 2010; Wilkinson, 2013; Arai and Miura, 2016; Holwell et al., 2017; Boudreau, 2019).

This conclusion contrasts with the behavior of gold, which exhibits a similar affinity as platinum for reduced sulfur (Pearson, 1968a,b, 1997; Cotton et al., 1988). Gold is much more soluble and mobile than platinum in most epithermal systems hosting large (10s to 100s tons) gold deposits (e.g., Kouzmanov and Pokrovski, 2012; references therein). In such fluids, the speciation of Au^{I} is largely dominated by similar hydrosulfide complexes, such as $Au(HS)_2^-$, commonly attaining ppm-level concentrations (Seward, 1973; Pokrovski et al., 2014, 2015). Paradoxically, the affinities of Pt^{II} and Au^{I}

to the aqueous HS^- ligand compared to Cl^- are very similar as can be quantified using the symmetrical ligand exchange reactions:

$$Au^{I}Cl_2^- + 2\ HS^- = Au^{I}(HS)_2^- + 2\ Cl^- \quad (12)$$

These reactions have equilibrium constant values ($\log_{10}K_{10}$ and $\log_{10}K_{11}$) of 23.2 and 11.4 at 300 °C and 500 bar. These values correspond to 5.8 and 5.7 per HS^- ligand, respectively, if normalized to the number of ligands in each complex. The major difference in the geochemical behavior of Au and Pt in hydrothermal systems is thus the difference in their stable solubility-controlling solid phases. The formation of platinum sulfide minerals (Fig. 1) makes Pt very poorly soluble compared to gold whose solubility is controlled by the native metal. If Pt metal were the stable phase in S-bearing environments, its solubility would be fairly comparable with that of gold (Fig. 7b). This difference in the solid-phase control on the metal transport is likely to be the main cause of the general scarcity of Pt and other PGE compared to Au in epithermal deposits of gold and base metals (e.g., Barnes and Liu, 2012; Kouzmanov and Pokrovski, 2012; Bazarkina et al., 2014; Pokrovski et al., 2014; Filimonova et al., 2021).

To account for Pt and other PGE mobility in hydrothermal fluids, complexes other than with HS^- or Cl^- would be required. The most plausible one, which is capable of strongly complexing Pt, is the trisulfur radical ion S_3^- that is abundant in sulfate-sulfide solutions over a wide range of temperatures (e.g., Pokrovski and Dubessy, 2015; Colin et al., 2020). Similar conclusions have been reached for Pd, whose Cl^- and HS^- complexes are equally too poorly soluble to account for significant Pd hydrothermal transport (Bazarkina et al., 2014). Extremely stable Pt-HS-S_3 mixed-ligand species were recently evidenced both for Pt^{II} and Pt^{IV} in S_3^--bearing fluids at 300 °C (Pokrovski et al., 2021). Work is currently in progress to extend these findings to a larger *T-P*-compositional range of hydrothermal-magmatic fluids. More generally, the results of the present study provide a basis for more systematic future

studies, using combined interdisciplinary experimental, spectroscopic and modeling approaches, of the role of hydrothermal fluids in the behavior of platinum group elements in nature.

7. CONCLUSIONS

We have performed, for the first time, a systematic study that combined solubility experiments, in situ X-ray absorption spectroscopy, and thermodynamic and molecular dynamics modeling to investigate platinum speciation in sulfide-bearing hydrothermal fluids. This unique combination enables more robust constraints on the nature and stability of Pt-HS complexes in hydrothermal fluids that would have been impossible using a single method.

The combination of MD simulations with both XANES and EXAFS structural analyses provides direct evidence that the tetrahydrosulfide species, $Pt(HS)_4^{2-}$, is the most stable one among the different Pt-HS complexes considered so far in moderate-temperature S-bearing hydrothermal fluids. Coupled with accurate solubility measurements using flexible cell hydrothermal reactors and in situ spectroscopy, our data allow generation of the stability constants for this Pt species over the temperature range of 50 to 300 °C and pressures <700 bar. The derived stability constants allow the solubility of Pt-bearing phases to be predicted in typical hydrothermal fluids below 350 °C. Solubility of PtS(s) appears, however, to be less than 0.1–1 ppb Pt, in contrast to much more soluble gold (ppm levels) despite the similar chemical affinities of both metals for reduced sulfur in aqueous solution. The major difference in PGE vs Au mobility is therefore the nature of the solubility-controlling phase, sulfide vs metal for Pt and Au, respectively. This difference is the key factor of Au vs PGE fractionation in hydrothermal systems.

The solubility of Pt as sulfide, chloride, sulfate or hydroxide complexes appears to be too low in typical moderate-temperature (≤350 °C) hydrothermal fluids to account for multiple instances of Pt remobilization and concentrations observed in natural settings. Complexes with other S-bearing

ligands, such as polysulfide dianions and radical sulfur ions, may significantly contribute to PGE fluid-phase mobility. Their studies in a wide *T-P*-compositional range of hydrothermal-magmatic fluids will require a combined experimental, spectroscopic and computational approach such as that developed in this study.

ACKNOWLEDGMENTS

This work was funded by the French National Research Agency (grant RadicalS – ANR-16-CE31-0017 to G.S.P.), the Institut Carnot ISIFoR (grants OrPet and AsCOCrit to G.S.P.), and the CNRS through the MITI interdisciplinary programs (grant PtS3-MetalloMix-2021 to G.S.P., J-L.H. and R.V.). The Institut Néel hydrothermal apparatus was financially supported by the French "grand emprunt" EquipEx (PlanEx, ANR-11-EQPX-36). C.L acknowledges support from the University of Toulouse (PhD fellowship of the Ministère de l'Enseignement Supérieur, de la Recherche et de l'Innovation, MESRI). We acknowledge the European Synchrotron Radiation Facility (ESRF) for providing access to beam time and infrastructure, and the OCCIGEN facility of Genopole (Evry, France) for providing computer time. We thank O. Proux, E. Lahera, J. Babinot, S. Foulon, K. Jaouen, P. Gisquet, A. Castillo, P. Bénézeth, C. Causserand, P. Besson, K. Alloncle, L. Menjot, M. Henry, A. Marquet, J. Chmeleff, A. Seitsonen, H. Müller, L. Bourcet, D. Testemale, and G. Berger for their advice and help with experiments and analyses. We are grateful to A. Migdisov and two anonymous referees for comments and X. Liu for editorial handling.

APPENDIX A. SUPPLEMENTARY MATERIAL

Supplementary material associated with this article can be found in the online version.

REFERENCES

Adamo C. and Barone V. (1999) Toward reliable density functional methods without adjustable parameters: The PBE0 model. *J. Chem. Phys.* **110**, 6158–6170.

Ahmadi T. S., Wang Z. L., Green T. C., Henglein A. and El-Sayed M. A. (1996) Shape-controlled synthesis of colloidal platinum nanoparticles. *Science* **272**, 1924–1925.

Akinfiev N. N. and Diamond L. W. (2003) Thermodynamic description of aqueous nonelectrolytes at infinite dilution over a wide range of state parameters. *Geochim. Cosmochim. Acta* **67**, 613–629.

Arai S. and Miura M. (2016) Formation and modification of chromitites in the mantle. *Lithos* **264**, 277–295.

Ayala R., Marcos E. S., Díaz-Moreno S., Solé V. A. and Muñoz-Páez A. (2001) Geometry and hydration structure of Pt (II) square planar complexes $[Pt(H_2O)_4]^{2+}$ and $[PtCl_4]^{2-}$ as studied by X-ray absorption spectroscopies and quantum-mechanical computations. *J. Phys. Chem. B* **105**, 7588–7593.

Ballhaus C. G. and Stumpfl E. F. (1986) Sulfide and platinum mineralization in the Merensky Reef:

Barnes S. J. and Liu W. (2012) Pt and Pd mobility in hydrothermal fluids: Evidence from komatiites and from thermodynamic modelling. *Ore Geol. Rev.* **44**, 49–58.

Barnes S.-J. and Ripley E. M. (2016) Highly siderophile and strongly chalcophile elements in magmatic ore deposits. *Rev. Mineral. Geochem.* **81**, 725–774.

Barnes S. J., Mungall J. E., Vaillant M. L., Godel B., Lesher C. M., Holwell D., Lightfoot P. C., Krivolutskaya N. and Wei B. (2017) Sulfide-silicate textures in magmatic Ni-Cu-PGE sulfide ore deposits: Disseminated and net-textured ores. *Am. Mineral.* **102**, 473–506.

Barré G., Truche L., Bazarkina E. F., Michels R. and Dubessy J. (2017) First evidence of the trisulfur radical ion S_3^- and other sulfur polymers in natural fluid inclusions. *Chem. Geol.* **462**, 1–14.

Bazarkina E. F., Pokrovski G. S., Zotov A. V. and Hazemann J.-L. (2010) Structure and stability of cadmium chloride complexes in hydrothermal fluids. *Chem. Geol.* **276**, 1–17.

Bazarkina E. F., Pokrovski G. S. and Hazemann J.-L. (2014) Structure, stability and geochemical role of palladium chloride complexes in hydrothermal fluids. *Geochim. Cosmochim. Acta* **146**, 107–131.

Boudreau A. (2019) *Hydromagmatic processes and platinum-group element deposits in layered intrusions*. Cambridge University Press.

Brenan J. M. (2008) The Platinum-Group Elements: "Admirably Adapted" for Science and Industry. *Elements* **4**, 227–232.

Brimhall G. H. and Crerar D. A. (1987) Ore fluids: magmatic to supergene. *Rev. Miner.* **17**, 235–265.

Bühl M., Kabrede H., Diss R. and Wipff G. (2006) Effect of hydration on coordination properties of uranyl (VI) complexes. A first-principles molecular dynamics study. *J. Am. Chem. Soc.* **128**, 6357–6368.

Bühl M., Sieffert N., Golubnychiy V. and Wipff G. (2008) Density functional theory study of uranium (VI) aquo chloro complexes in aqueous solution. *J. Phys. Chem. A* **112**, 2428–2436.

Bunău O. and Joly Y. (2009) Self-consistent aspects of X-ray absorption calculations. *J. Phys. Condens. Matter* **21**, 345501.

Bussi G., Donadio D. and Parrinello M. (2007) Canonical sampling through velocity rescaling. *J. Chem. Phys.* 126, 014101.

Car R. and Parrinello M. (1985) Unified approach for molecular dynamics and density-functional theory. *Phys. Rev. Lett.* **55**, 2471.

Chen K., Walker R. J., Rudnick R. L., Gao S., Gaschnig R. M., Puchtel I. S., Tang M. and Hu Z.-C. (2016) Platinum-group element abundances and Re–Os isotopic systematics of the upper continental crust through time: Evidence from glacial diamictites. *Geochim. Cosmochim. Acta* **191**, 1–16.

Chong L., Wen J., Kubal J., Sen F. G., Zou J., Greeley J., Chan M., Barkholtz H., Ding W. and Liu D.-J. (2018) Ultralow-loading platinum-cobalt fuel cell catalysts derived from imidazolate frameworks. *Science* **362**, 1276–1281.

Colin A., Schmidt C., Pokrovski G. S., Wilke M., Borisova A. Y. and Toplis M. J. (2020) *In situ* determination of sulfur speciation and partitioning in aqueous fluid-silicate melt systems. *Geochem. Persp. Let.* **14**, 31–35.

Cotton F. A., Wilkinson G., Murillo C. A., Bochmann M. and Grimes R. (1988) *Advanced Inorganic Chemistry*., Wiley, New York.

Crowther N. (2007) Catalyseurs à base de complexes de platine incorporés dans les murs de silices mesoporeuses périodiques; réactivité en hydrogénation. Ph. D. Thesis, Ecole normale supérieure de lyon.

Da Silva C., Proux O., Hazemann J.-L., James-Smith J., Testemale D. and Yamaguchi T. (2009) X-ray absorption spectroscopy study of solvation and ion-pairing in aqueous gallium bromide solutions at supercritical conditions. *J. Mol. Liq.* **147**, 83–95.

Duran C. J., Barnes S.-J., Pleše P., Kudrna Prašek M., Zientek M. L. and Pagé P. (2017) Fractional crystallization-induced variations in sulfides from the Noril'sk-Talnakh mining district (polar Siberia, Russia). *Ore Geol. Rev.* **86**, 529–552.

Economou-Eliopoulos M. (2010) Platinum-group elements (PGE) in various geotectonic settings: opportunities and risks. *Hell. J. Geosci.* **45**, 65–82.

Elding L. I. (1972a) Palladium (II) halide complexes. I. Stabilities and spectra of palladium (II) chloro and bromo aqua complexes. *Inorganica Chim. Acta* **6**, 647–651.

Elding L. I. (1972b) Palladium (II) halide complexes, II. Acid hydrolyses and halide anations of palladium (II) chloro and bromo aqua complexes. *Inorganica Chim. Acta* **6**, 683–688.

Elding L. I. (1978) Stabilities of platinum (II) chloro and bromo complexes and kinetics for anation of the tetraaquaplatinum (II) ion by halides and thiocyanate. *Inorg. Chim. Acta* **28**, 255–262.

Filimonova O. N., Nickolsky M. S., Trigub A. L., Chareev D. A., Kvashnina K. O., Kovalchuk E. V., Vikentyev I. V. and Tagirov B. R. (2019) The state of platinum in pyrite studied by X-ray absorption spectroscopy of synthetic crystals. *Econ. Geol.* **114**, 1649–1663.

Filimonova O. N., Tagirov B. R., Zotov A. V., Baranova N. N., Bychkova Y. V., Tyurin D. A., Chareev D. A. and Nickolsky M. S. (2021) The solubility of cooperite PtS(cr) at 25 – 450 °C, Psat – 1000 bar and hydrosulfide complexing of platinum in hydrothermal fluids. *Chem. Geol.* **559**, 119968.

Gammons C. H. and Bloom M. S. (1993) Experimental investigation of the hydrothermal geochemistry of platinum and palladium: II. The solubility of PtS and PdS in aqueous sulfide solutions to 300°C. *Geochim. Cosmochim. Acta* **57**, 2451–2467.

Gœdecker S., Teter M. and Hutter J. (1996) Separable dual-space Gaussian pseudopotentials. *Phys. Rev. B* **54**, 1703.

Gorczyca A., Moizan V., Chizallet C., Proux O., Del Net W., Lahera E., Hazemann J.-L., Raybaud P. and Joly Y. (2014) Monitoring morphology and hydrogen coverage of nanometric Pt/γ-Al_2O_3 particles by in situ HERFD–XANES and quantum simulations. *Angew. Chem.* **126**, 12634–12637.

Grimme S. (2006) Semiempirical GGA-type density functional constructed with a long-range dispersion correction. *J. Comput. Chem.* **27**, 1787-1799..

Grønvold F., Haraldsen H. and Kjekshus A. (1960) On the sulfides, selenides and tellurides of platinum. *Acta Chem Scand* **14**, 1879–1893.

Guan Q., Mei Y., Etschmann B., Testemale D., Louvel M. and Brugger J. (2020) Yttrium complexation and hydration in chloride-rich hydrothermal fluids: A combined ab initio molecular dynamics and in situ X-ray absorption spectroscopy study. *Geochim. Cosmochim. Acta* **281**, 168–189.

Hanley J. J. (2005) The aqueous geochemistry of the platinum-group elements (PGE) in surficial, low-T hydrothermal and high-T magmatic-hydrothermal environments. In *Exploration for Platinum Group Elements Deposits* (ed. J. E. Mungall). Min. Assoc. Canada Short Course **35**, 35–56.

Hartwigsen C., Gœdecker S. and Hutter J. (1998). Relativistic separable dual-space Gaussian pseudopotentials from H to Rn. *Phys. Rev. B* **58**, 3641.

Holwell D. A., Adeyemi Z., Ward L. A., Smith D. J., Graham S. D., McDonald I. and Smith J. W. (2017) Low temperature alteration of magmatic Ni-Cu-PGE sulfides as a source for hydrothermal Ni and PGE ores: A quantitative approach using automated mineralogy. *Ore Geol. Rev.* **91**, 718–740.

Hou R., Quan Y. and Pan D. (2020) Dielectric constant of supercritical water in a large pressure–temperature range. *J. Chem. Phys.* **153**, 101103.

Hutchinson D. and Kinnaird J. A. (2005) Complex multistage genesis for the Ni–Cu–PGE mineralisation in the southern region of the Platreef, Bushveld Complex, South Africa. *Appl. Earth Sci.* **114**, 208–224.

Johnson J. W., Oelkers E. H. and Helgeson H. C. (1992) SUPCRT92: A software package for calculating the standard molal thermodynamic properties of minerals, gases, aqueous species, and reactions from 1 to 5000 bar and 0 to 1000°C. *Comput. Geosci.* **18**, 899–947.

Joly Y. (2001) X-ray absorption near-edge structure calculations beyond the muffin-tin approximation. *Phys. Rev. B* **63**, 125120.

Kamitpanjadharesh W. and Boudreau A. E. (2013) Sulfide associated mineral assemblages in the Bushveld Complex, South Africa: platinum-group element enrichment by vapor refining by chloride–carbonate fluids. *Miner. Deposita* **48**, 193–210.

Karzhavin V. K. (2007) Sulfides, selenides, and tellurides of platinum and palladium: Estimation of thermodynamic properties. *Geochem. Int.* **45**, 931–937.

Kelly S. D., Hesterberg D. and Ravel B. (2008) Analysis of soils and minerals using X-ray absorption spectroscopy. *Methods Soil Anal. Part 5 Mineral. Methods* **5**, 387–464.

Kerr A. and Leitch A. M. (2005) Self-destructive sulfide segregation systems and the formation of high-grade magmatic ore deposits. *Econ. Geol.* **100**, 311–332.

Kim K., Kim H.-T. and Han J.-I. (2015) Compatibility of platinum with alkaline sulfide fuel: effectiveness and stability of platinum as an anode catalyst in direct alkaline sulfide fuel cell. *Int. J. Hydrog. Energy* **40**, 4141–4145.

Kleine B. I., Gunnarsson-Robin J., Kamunya K. M., Ono S. and Stefánsson A. (2021) Source controls on sulfur abundance and isotope fractionation in hydrothermal fluids in the Olkaria geothermal field, Kenya. *Chem. Geol.* **582**, 120446.

Kokh M. A., Akinfiev N. N., Pokrovski G. S., Salvi S. and Guillaume D. (2017) The role of carbon dioxide in the transport and fractionation of metals by geological fluids. *Geochim. Cosmochim. Acta* **197**, 433–466.

Kokh M.A., Assayag N., Mounic S., Cartigny P., Gurenko A., Pokrovski G.S. (2020) Multiple sulfur isotope fractionation in hydrothermal systems in the presence of radical ions and molecular sulfur. *Geochim. Cosmochim. Acta* **285**, 100-128.

Kouzmanov K., Pokrovski G.S. (2012) Hydrothermal controls on metal distribution in Cu(-Au-Mo) porphyry systems. Book chapter in: Geology and Genesis of Geology and Genesis of Major Copper Deposits and Districts of the World: A Tribute to Richard H. Sillitoe (eds. J.W. Hedenquist, M. Harris, and F. Camus). *Society of Economic Geologists Spec. Pub.*, **16**, 573-618.

Krack M. (2005) Pseudopotentials for H to Kr optimized for gradient-corrected exchange-correlation functionals. *Theor. Chem. Acc.* **114**, 145-152.

Kühne T. D., Iannuzzi M., Del Ben M., Rybkin V. V., Seewald P., Stein F., Laino T., Khaliullin R. Z., Schütt O., Schiffmann F., Golze D., Wilhelm J., Chulkov S., Bani-Hashemian M. H., Weber V., Borštnik U., Taillefumier M., Jakobovits A. S., Lazzaro A., Pabst H., Müller T., Schade R., Guidon M., Andermatt S., Holmberg N., Schenter G. K., Hehn A., Bussy A., Belleflamme F., Tabacchi G., Glöß A., Lass M., Bethune I., Mundy C. J., Plessl C., Watkins M., VandeVondele J., Krack M. and Hutter J. (2020) CP2K: An electronic structure and molecular dynamics software package - Quickstep: Efficient and accurate electronic structure calculations. *J. Chem. Phys.* **152**, 194103.

Laskar C. (2022) Impact du soufre sur le transport des platinoïdes par les fluides hydrothermaux. Ph. D. thesis, Univ. de Toulouse.

Le Vaillant M., Barnes S. J., Fiorentini M. L., Santaguida F. and Törmänen T. (2016a) Effects of hydrous alteration on the distribution of base metals and platinum group elements within the Kevitsa magmatic nickel sulphide deposit. *Ore Geol. Rev.* **72**, 128–148.

Le Vaillant M., Saleem A., Barnes S. J., Fiorentini M. L., Miller J., Beresford S. and Perring C. (2016b) Hydrothermal remobilisation around a deformed and remobilised komatiite-hosted Ni-Cu-(PGE) deposit, Sarah's Find, Agnew Wiluna greenstone belt, Yilgarn Craton, Western Australia. *Miner. Deposita* **51**, 369–388.

Lee I., Morales R., Albiter M. A. and Zaera F. (2008) Synthesis of heterogeneous catalysts with well shaped platinum particles to control reaction selectivity. *Proc. Natl. Acad. Sci.* **105**, 15241–15246.

Li Y., Zhou S., Li J., Ma Y., Chen K., Wu Y. and Zhang Y. (2017) Experimental study of the decomposition of acetic acid under conditions relevant to deep reservoirs. *Appl. Geochem.* **84**, 306–313.

Liu W., Etschmann B., Mei Y., Guan Q., Testemale D. and Brugger J. (2020) The role of sulfur in molybdenum transport in hydrothermal fluids: insight from in situ synchrotron XAS experiments and molecular dynamics simulations. *Geochim. Cosmochim. Acta* **290**, 162–179.

Lorand J.-P., Luguet A. and Alard O. (2008) Platinum-group elements: a new set of key tracers for the Earth's interior. *Elements* **4**, 247–252.

Luguet A., Pearson D. G., Nowell G. M., Dreher S. T., Coggon J. A., Spetsius Z. V. and Parman S. W. (2008) Enriched Pt-Re-Os isotope systematics in plume lavas explained by metasomatic sulfides. *Science* **319**, 453–456.

Mcmahon G., Oberthur T., Cabri L. J., Weisner T. W., McMahon G. and Muller P. (1997) Pt, Pd and other trace elements in sulfides of the main sulfide zone, Great Dyke, Zimbabwe: a reconnaissance study. *Can. Mineral.* **35**, 597–609.

Mei Y., Sherman D. M., Liu W. and Brugger J. (2013a) Ab initio molecular dynamics simulation and free energy exploration of copper(I) complexation by chloride and bisulfide in hydrothermal fluids. *Geochim. Cosmochim. Acta* **102**, 45–64.

Mei Y., Sherman D. M., Liu W. and Brugger J. (2013b) Complexation of gold in S3−-rich hydrothermal fluids: Evidence from ab-initio molecular dynamics simulations. *Chem. Geol.* **347**, 34–42.

Mei Y., Liu W., Sherman D. M. and Brugger J. (2014) Metal complexation and ion hydration in low density hydrothermal fluids: ab initio molecular dynamics simulation of Cu(I) and Au(I) in chloride solutions (25–1000°C, 1–5000bar). *Geochim. Cosmochim. Acta* **131**, 196–212.

Mei Y., Etschmann B., Liu W., Sherman D. M., Barnes S. J., Fiorentini M. L., Seward T. M., Testemale D. and Brugger J. (2015a) Palladium complexation in chloride- and bisulfide-rich fluids: insights from ab initio molecular dynamics simulations and X-ray absorption spectroscopy. *Geochim. Cosmochim. Acta* **161**, 128–145.

Mei Y., Sherman D. M., Liu W., Etschmann B., Testemale D. and Brugger J. (2015b) Zinc complexation in chloride-rich hydrothermal fluids (25–600 °C): a thermodynamic model derived from ab initio molecular dynamics. *Geochim. Cosmochim. Acta* **150**, 265–284.

Mei Y., Etschmann B., Liu W., Sherman D. M., Testemale D. and Brugger J. (2016) Speciation and thermodynamic properties of zinc in sulfur-rich hydrothermal fluids: Insights from ab initio molecular dynamics simulations and X-ray absorption spectroscopy. Geochim. Cosmochim. Acta 179, 32–52.

Mei Y. (2020) Gold solubility in alkaline and ammonia-rich hydrothermal fluids: Insights from ab initio molecular dynamics simulations. *Geochim. Cosmochim. Acta*, 17.

Moldovan M., Palacios M. A., Gomez M. M., Morrison G., Rauch S., McLeod C., Ma R., Caroli S., Alimonti A. and Petrucci F. (2002) Environmental risk of particulate and soluble platinum group elements released from gasoline and diesel engine catalytic converters. *Sci. Total Environ.* **296**, 199–208.

Mudd G. M. and Jowitt S. M. (2014) A Detailed Assessment of Global Nickel Resource Trends and Endowments. *Econ. Geol.* **109**, 1813–1841.

Mungall J. E., Ed. (2005), Exploration for platinum-group elements deposits. *Min. Assoc. Canada Short Course* **35**, 1−494.

Mungall J. E. and Naldrett A. J. (2008) Ore deposits of the platinum-group elements. *Elements* **4**, 253–258.

Neese F. (2012) The ORCA program system. *Wiley Interdiscip. Rev. Comput. Mol. Sci.* **2**, 73–78.

Neese F. (2018) Software update: the ORCA program system, version 4.0. *Wiley Interdiscip. Rev. Comput. Mol. Sci.* **8**, e1327.

Newville M. (2001) IFEFFIT: interactive XAFS analysis and FEFF fitting. *J. Synchrotron Radiat.* **8**, 322–324.

Oelkers E. H., Benezeth P. and Pokrovski G. S. (2009) Thermodynamic databases for water-rock interaction. *Rev. Mineral. Geochem.* **70**, 1–46.

Palme H. (2008) Platinum-group elements in cosmochemistry. *Elements* **4**, 233–238.

Pan Y. and Wood S. A. (1994) Solubility of Pt and Pd sulfides and Au metal in aqueous bisulfide solutions: II. Results at 200° to 350°C and saturated vapor pressure. *Miner. Deposita* **29**, 373–390.

Pearson R. G. (1997) *Chemical Hardness*. Wiley Online Library.

Pearson R. G. (1968a) Hard and soft acids and bases, HSAB, part 1: Fundamental principles. *J. Chem. Educ.* **45**, 581–587.

Pearson R. G. (1968b) Hard and soft acids and bases, HSAB, part II: Underlying theories. *J. Chem. Educ.* **45**, 643–648.

Perdew J. P., Burke K. and Ernzerhof M. (1996) Generalized gradient approximation made simple. *Phys. Rev. Lett.* **77**, 3865–3868.

Perdew J. P. and Levy M. (1997) Comment on "Significance of the highest occupied Kohn-Sham eigenvalue." *Phys. Rev. B* **56**, 16021–16028.

Peyrelade E. (2005) Élaborations et caractérisations électrochimiques et physiques de matériaux d'anode de PEMFC peu sensibles à l'empoisonnement par CO: étude d'alliages et de composites à base de platine-molybdène et de platine-tungstène. Ph. D. thesis., Institut National Polytechnique de Grenoble.

Phillips D. J. and Phillips S. L. (2000) High temperature dissociation constants of HS^- and the standard thermodynamic values for S^{2-}. *J. Chem. Eng. Data* **45**, 981–987.

Pokrovski G. S. and Dubessy J. (2015) Stability and abundance of the trisulfur radical ion S_3^- in hydrothermal fluids. *Earth Planet. Sci. Lett.* **411**, 298–309.

Pokrovski G. S., Roux J., Hazemann J.-L. and Testemale D. (2005) An X-ray absorption spectroscopy study of argutite solubility and aqueous Ge(IV) speciation in hydrothermal fluids to 500 °C and 400 bar. *Chem. Geol.* **217**, 127–145.

Pokrovski G. S., Borisova A. Yu., Roux J., Hazemann J.-L., Petdang A., Tella M. and Testemale D. (2006) Antimony speciation in saline hydrothermal fluids: a combined X-ray absorption fine structure spectroscopy and solubility study. *Geochim. Cosmochim. Acta* **70**, 4196–4214.

Pokrovski G. S., Borisova A. Yu. and Harrichoury J.-C. (2008) The effect of sulfur on vapor–liquid fractionation of metals in hydrothermal systems. *Earth Planet. Sci. Lett.* **266**, 345–362.

Pokrovski G. S., Tagirov B. R., Schott J., Bazarkina E. F., Hazemann J.-L. and Proux O. (2009) An in situ X-ray absorption spectroscopy study of gold-chloride complexing in hydrothermal fluids. *Chem. Geol.* **259**, 17–29.

Pokrovski G. S., Akinfiev N. N., Borisova A. Y., Zotov A. V. and Kouzmanov K. (2014) Gold speciation and transport in geological fluids: insights from experiments and physical-chemical modelling. *Geol. Soc. Lond. Spec. Publ.* **402**, 9–70.

Pokrovski G. S., Kokh M. A., Guillaume D., Borisova A. Y., Gisquet P., Hazemann J.-L., Lahera E., Del Net W., Proux O., Testemale D., Haigis V., Jonchière R., Seitsonen A. P., Ferlat G., Vuilleumier R., Saitta A. M., Boiron M.-C. and Dubessy J. (2015) Sulfur radical species form gold deposits on Earth. *Proc. Natl. Acad. Sci.* **112**, 13484–13489.

Pokrovski G. S., Kokh M. A., Desmaele E., Laskar C., Bazarkina E. F., Borisova A. Y., Testemale D., Hazemann J.-L., Vuilleumier R., Ferlat G. and Saitta A. M. (2021) The trisulfur radical ion $S_3^{\bullet-}$ controls platinum transport by hydrothermal fluids. *Proc. Natl. Acad. Sci.* **118**, e2109768118.

Pokrovski G.S., Desmaele E., Laskar C., Bazarkina E.F., Testemale D., Hazemann J.-L., Vuilleumier R., Seitsonen A.P., Ferlat G., Saitta A.M. (2022) Gold speciation in hydrothermal fluids revealed by in situ high energy resolution X-ray absorption spectroscopy. *Am. Min.* **107**, 369-376.

Proux O., Biquard X., Lahera E., Menthonnex J. J., Prat A., Ulrich O., Soldo Y., Trvisson P., Kapoujyan G., Perroux G., Taunier P., Grand D., Jeantet P., Deleglise M., Roux Jp. and Hazemann Jl. (2005) FAME a new beamline for X-ray absorption investigations of very diluted systems of environmental, material and biological interests. *Phys. Scr.* **2005**, 970–973.

Ramachandran K. I., Deepa G. and Namboori K. (2008) *Computational Chemistry and Molecular Modeling: Principles and Applications*, Springer Science & Business Media, Berlin.

Ravel B. and Newville M. (2005) *ATHENA* , *ARTEMIS* , *HEPHAESTUS* : data analysis for X-ray absorption spectroscopy using *IFEFFIT*. *J. Synchrotron Radiat.* **12**, 537–541.

Rehkämper M., Halliday A. N., Barfod D., Fitton J. G. and Dawson J. B. (1997) Platinum-group element abundance patterns in different mantle environments. *Science* **278**, 1595–1598.

Resat H. and Mezei M. (1993) Studies on free energy calculations. I. Thermodynamic integration using a polynomial path. *J. Chem. Phys.* **99**, 6052–6061.

Rosenbauer R. J., Bischoff J. L. and Potter J. M. (1993) A flexible Au-Ir cell with quick assembly for hydrothermal experiments. *Am. Mineral.* **78**, 1286–1289.

Sassani D. C. and Shock E. L. (1998) Solubility and transport of platinum-group elements in supercritical fluids: summary and estimates of thermodynamic properties for ruthenium, rhodium, palladium, and platinum solids, aqueous ions, and complexes to 1000°C and 5 kbar. *Geochim. Cosmochim. Acta* **62**, 2643–2671.

Scholten L., Watenphul A., Beermann O., Testemale D., Ames D. and Schmidt C. (2018) Nickel and platinum in high-temperature H_2O + HCl fluids: implications for hydrothermal mobilization. *Geochim. Cosmochim. Acta* **224**, 187–199.

Seward T. M. (1973) Thio complexes of gold and the transport of gold in hydrothermal ore solutions. *Geochim. Cosmochim. Acta* **37**, 379–399.

Shvarov Yu. V. (2008) HCh: New potentialities for the thermodynamic simulation of geochemical systems offered by windows. *Geochem. Int.* **46**, 834–839.

Shvarov Y. (2015) A suite of programs, OptimA, OptimB, OptimC, and OptimS compatible with the Unitherm database, for deriving the thermodynamic properties of aqueous species from solubility, potentiometry and spectroscopy measurements. *Applied Geochem.* **55**, 17–27.

Spezia R., Bresson C., Auwer C. D. and Gaigeot M.-P. (2008) Solvation of Co (III)-Cysteinato Complexes in Water: A DFT-based Molecular Dynamics Study. *J. Phys. Chem. B* **112**, 6490–6499.

Spezia R., Beuchat C., Vuilleumier R., D'Angelo P. and Gagliardi L. (2012) Unravelling the hydration structure of ThX4 (X= Br, Cl) water solutions by molecular dynamics simulations and X-ray absorption spectroscopy. *J. Phys. Chem. B* **116**, 6465–6475.

Sprik M. and Ciccotti G. (1998) Free energy from constrained molecular dynamics. *J. Chem. Phys.* **109**, 7737–7744.

Steudel R. and Chivers T. (2019) The role of polysulfide dianions and radical anions in the chemical, physical and biological sciences, including sulfur-based batteries. *Chem. Soc. Rev.* **48**, 3279–3319.

Sullivan N. A., Zajacz Z., Brenan J. M., Hinde J. C., Tsay A. and Yin Y. (2022a) The solubility of gold and palladium in magmatic brines: Implications for PGE enrichment in mafic-ultramafic and porphyry environments. *Geochim. Cosmochim. Acta* **316**, 230–252.

Sullivan N. A., Zajacz Z., Brenan J. M. and Tsay A. (2022b) The solubility of platinum in magmatic brines: Insights into the mobility of PGE in ore-forming environments. *Geochim. Cosmochim. Acta* **316**, 253–272.

Sverjensky D. A. (2019) Thermodynamic modelling of fluids from surficial to mantle conditions. *J. Geol. Soc.* **176**, 348–374.

Tagirov B. R., Zotov A. V. and Akinfiev N. N. (1997) Experimental study of dissociation of HCl from 350 to 500°C and from 500 to 2500 bars: Thermodynamic properties of HCl^0(aq). *Geochim. Cosmochim. Acta* **61**, 4267–4280.

Tagirov B. R., Baranova N. N. and Bychkova Y. V. (2015) Thermodynamic properties of platinum chloride complexes in aqueous solutions: Derivation of consistent parameters from literature data and experiments on Pt(cr) solubility at 400–475°C and 1 kbar. *Geochem. Int.* **53**, 327–340.

Tagirov B. R., Filimonova O. N., Trigub A. L., Akinfiev N. N., Nickolsky M. S., Kvashnina K. O., Chareev D. A. and Zotov A. V. (2019) Platinum transport in chloride-bearing fluids and melts: insights from in situ X-ray absorption spectroscopy and thermodynamic modeling. *Geochim. Cosmochim. Acta* **254**, 86–101.

Tanger J. C. and Helgeson H. C. (1988) Calculation of the thermodynamic and transport properties of aqueous species at high pressures and temperatures; revised equations of state for the standard partial molal properties of ions and electrolytes. *Am. J. Sci.* **288**, 19–98.

Testemale D., Argoud R., Geaymond O. and Hazemann J.-L. (2005) High pressure/high temperature cell for X-ray absorption and scattering techniques. *Rev. Sci. Instrum.* **76**, 043905.

Tödheide K. (1982) Hydrothermal solutions. *Ber. Buns. Phys. Chem.* **86**, 1005–1016.

Trofimov B. A., Sinegovskaya L. M. and Gusarova N. K. (2009) Vibrations of the S–S bond in elemental sulfur and organic polysulfides: a structural guide. *J. Sulfur Chem.* **30**, 518–554.

VandeVondele J. and Hutter J. (2007) Gaussian basis sets for accurate calculations on molecular systems in gas and condensed phases. *J. Chem. Phys.* **127**, 114105.

Vícha J., Novotný J., Straka M., Repisky M., Ruud K., Komorovsky S. and Marek R. (2015) Structure, solvent, and relativistic effects on the NMR chemical shifts in square-planar transition-metal complexes: assessment of DFT approaches. *Phys. Chem. Chem. Phys.* **17**, 24944–24955.

Wallace P. J. (2005) Volatiles in subduction zone magmas: concentrations and fluxes based on melt inclusion and volcanic gas data. *J. Volcanol. Geotherm. Res.* **140**, 217–240.

Walther J. V. and Schott J. (1988) The dielectric constant approach to speciation and ion pairing at high temperature and pressure. *Nature* **332**, 635–638.

Wickenden A. E. and Krause R. A. (1969) Polysulfide chelates. II. Desulfuration of PtS_{15}^{2-} and the synthesis of PtS_{10}^{2-}. *Inorg. Chem.* **8**, 779–783.

Wilkinson J. J. (2013) Triggers for the formation of porphyry ore deposits in magmatic arcs. *Nat. Geosci.* **6**, 917–925.

Wood S. A. and (2002) The aqueous geochemistry of the platinum-group elements with applications to ore deposits. In *The Geology, Geochemistry, Mineralogy and Mineral Beneficiation of Platinum-Group Elements* (ed. L. J. Cabri). Canadian Institute of Mining, Metallurgy and Petroleum Special, vol. 54, pp. 211–249.

Zajacz Z., Seo J. H., Candela P. A., Piccoli P. M., Heinrich C. A. and Guillong M. (2010) Alkali metals control the release of gold from volatile-rich magmas. *Earth Planet. Sci. Lett.* **297**, 50–56.

Zajacz Z., Seo J. H., Candela P. A., Piccoli P. M. and Tossell J. A. (2011) The solubility of copper in high-temperature magmatic vapors: A quest for the significance of various chloride and sulfide complexes. *Geochim. Cosmochim. Acta* **75**, 2811–2827.

Zientek M. L. (2012) *Magmatic ore deposits in layered intrusions: Descriptive model for reef-type PGE and contact-type Cu-Ni-PGE deposits*. U.S. Geological Survey Open-File Report 2012–1010.

Zimmer K., Zhang Y., Lu P., Chen Y., Zhang G., Dalkilic M. and Zhu C. (2016) SUPCRTBL: A revised and extended thermodynamic dataset and software package of SUPCRT92. *Comput. Geosci.* **90**, 97-111.

TABLES AND FIGURES

Table 1. Platinum dissolved concentration and fluid composition and major parameters in the system H_2O-NaHS-PtS-Au-FeS-FeS_2 at the indicated *T-P* conditions during the different steps of FCR experiment m35.

Run/step	*T*, °C	*P*, bar	NaHS, m	$H_2S_{(aq)}$, m	HCl, m	NaOH, m	H_2O_2, m	pH[a]	$\log_{10} f_{O_2}$[a]	$m_{Pt,\,mean}$ (×10^6), m	$\log_{10}\beta_4$	N_{exp}	Injected aqueous solution
m35/1	56	320±5	1.04	0.12	–	–	–	7.8	–78	14	–17.3	1	–
m35/10	50	260±10	0.51	0.07	0.48	–	–	5.3	–80	0.11	–17.2	3	–
m35/11	50	440±5	0.51	0.07	0.48	–	–	5.3	–80	0.28	–17.1	2	–
m35/12[b,d]	50	90±10	0.51	0.07	0.48	–	–	5.4	–80	3.8[b,d]	–[b]	2	–
m35/13	50	250±5	0.44	0.06	0.41	0.04	–	5.8	–80	2.3	–16.6	2	NaOH
m35/14[d]	50	260±5	0.15[c]	0.05	0.35	0.03	0.29	6.4	–65	2.9[d]	–15.8[d]	2	H_2O_2
m35/9	100	250±5	0.51	0.07	0.48	–	–	5.0	–67	0.12	–16.7	3	–
m35/2	200	470±40	1.04	0.12	–	–	–	7.1	–49	3.4	–17.9	2	–
m35/8	200	300±50	0.51	0.07	0.48	–	–	5.0	–50	0.21	–16.8	2	H_2O
m35/3	250	510±70	1.04	0.12	–	–	–	7.3	–42	3.1	–18.4	4	–
m35/7	250	400±100	0.67	0.09	0.62	–	–	5.3	–43	0.60	–17.5	5	H_2O
m35/4	300	470±50	1.04	0.12	–	–	–	7.5	–36	3.3	–19.0	3	–
m35/5	300	450±30	1.01	0.11	0.29	–	–	6.8	–37	4.0	–18.9	2	HCl
m35/6	300	490±40	0.81	0.10	0.71	–	–	5.7	–38	0.68	–18.5	3	HCl
Error	±1		±10%	±10%	±5%	±5%	±5%	±0.1	±1	±10%	±0.5		

m denotes the number of moles of each solute per kg of water (mol/kg H_2O); N_{exp} corresponds to the number of samples for used to calculate the average value, $m_{Pt,mean}$; the x number in m35/x (1≤x≤14) represents the chronological order of the corresponding step; *P* is reported as the mean value with 1 standard deviation accounting for pressure variations during a given step. See Table S1 for further analytical details.

[a] pH and f_{O_2} are calculated from the composition of the experiment at different steps with the HCh software.

[b] samples are likely not representative because of a suspected cell leak at this step; they were ignored in further interpretation.

[c] injection of H_2O_2 solution makes some sulfur $S_{8,liq}$ (0.18 mol) to form in the system.

[d] not considered in the thermodynamic analysis.

Table 2. Platinum concentrations and fluid compositions in XAS experiments at the indicated *T*-*P* conditions. Pt concentration were determined at the Pt-L_{III} absorption edge from fluorescence signals.

#	Composition	duration, hours	*T*, °C	*P*, bar	pH[a]	$\log_{10} f_{O_2}$[a]	$\Delta\mu_{fluo} \times 10^3$	d_{fluid}, g/cm^3	m_{Pt}[b] (×10^6), m	$\log_{10} \beta_4$
Exp1	NaHS (2.03 m) + H_2S (0.07 m)	14.0	250	500	7.7	–39	0.19±0.02	0.93	9.1±0.8	–18.3
Exp3	CH_3CNH_2S (2.16 m)	14.0	250	500	5.4	–41	1.9±0.1	1.00	90±20	–17.0
Exp4	NaHS (2.03 m) + H_2S (0.01 m)	17.6	300	500	8.4	–35	0.62±0.05	0.87	36±2	–17.8
Exp6	CH_3CNH_2S (2.35 m) + HCl (1.00 m)	14.5	300	500	5.0	–36	0.29±0.05	0.99	16±2	–17.4
Exp7	NaHS (0.97 m) + H_2S (0.01 m)	13.6	300	500	8.3	–35	0.16±0.01	0.83	6.5±0.5	–17.9
Exp8	CH_3CNH_2S (2.16 m)	13.6	300	500	5.4	–36	0.24±0.05	0.95	10±2	–18.1
Exp9	NaHS (2.02 m) + NaOH (0.58 m) + H_2S (0.01 m)	16.6	300	500	10.0	–36	0.15±0.02	0.89	8.2±0.8[b]	–16.8[b]
Error			±1	±10	±0.1	±1		±0.03		±0.5

Fluorescence calibration were performed with aqueous solutions of K_2PtCl_4, taking into account the absorption of the fluid and the distance of the sample to the detector (see Appendix A); m denotes the number of moles of each solute per kg of water (mol/kg H_2O).

[a] pH and f_{O_2} are calculated from the composition at the experimental *T*-*P* using the HCh software.

[b] not taken into account in the thermodynamic analysis of $Pt(HS)_4^{2-}$.

Table 3. Solution compositions, temperature, pressure and density of Pt^{II}-HS solutions used in the FPMD simulations of this study.

Job No.	Solution composition	*T*, °C	*P*, bar	Density, g/cm^3	Reaction	$\log_{10}K_x$
1	1 Pt, 1 HS, 131 H_2O	300	700	0.82	$Pt^{2+} + HS^- = Pt(HS)^+$	9.0±1.0
2	1 Pt, 2 HS, 130 H_2O	300	600	0.82	$Pt(HS)^+ + HS^- = Pt(HS)_2^0$	9.6±0.8
3	1 Pt, 3 HS, 129 H_2O	300	550	0.83	$Pt(HS)_2^0 + HS^- = Pt(HS)_3^-$	10.5±0.9
4	1 Pt, 4 HS, 128 H_2O	300	500	0.84	$Pt(HS)_3^- + HS^- = Pt(HS)_4^{2-}$	6.8±1.0

The cubic box size is 17.0 Å for all jobs. Errors on *P* and density are ±50 bar and ±0.03 g/cm^3, respectively.

Table 4. In situ platinum local atomic structure in sulfur-bearing aqueous solutions in equilibrium with PtS(s) derived from EXAFS modeling.

T, °C	*P*, bar	Atom	N	R, Å	σ², Å²	ΔE, eV	Reduced χ² (*R*-factor)	k-range, Å^{-1}	R-range, Å
250	500	S	4.0±0.5	2.30±0.01	0.003±0.001	7±1	33	3.0–11.5	1.2–5.0
		S_{fwa}		4.60[a]	0.011±0.005		(0.027)		

S_0^2 is the amplitude reduction factor set to 0.8; uncertainties are calculated by the ARTEMIS program; the number of variables (5) is lower than the number of independent points (20) for the fit; R = Pt-indicated atom mean distance; N = Pt-indicated atom coordination number; σ² = mean square displacement bond length (or Debye-Waller factor); ΔE is a non-structural parameter accounting for phase shift between experimental spectrum and FEFF calculation; *R*-factor defines goodness of the total fit in R-space; S_{fwa} = multiple scattering linear path forward through absorber (fwa) within the square $Pt(S)_4$ unit: Pt-S-Pt-S-Pt; $R(S_{fwa})=2\times R(S)$.

Table 5. Values of the PtS(s) dissolution reaction constants with different Pt-HS complexes at the indicated *T-P* conditions.

Reaction			$\log_{10}\beta_x(T,P)$		$\log_{10}\beta_x(T,P)$		$\log_{10}\beta_x(T,P)$	
			This study		Recalculated		Originally reported data (solubility)	
	T, °C	*P*, bar	FCR+XAS	FPMD	GB93[a]	PW94[a]	GB93[a]	F21[b]
	50	300	–17.1±0.5	–	–	–	–	–
	100	300	–16.7±0.5	–	–	–	–	–
$PtS + 3\ H_2S_{(aq)} = Pt(HS)_4^{2-} + 2\ H^+$	200	500	–17.4±0.5	–	–16.8±0.7	–17.8±1.6	–18.7±0.6	–
	250	500	–18.0±0.5	–	–18.6±0.5	–19.0±1.6	–20.4±0.5	–
	300	500	–18.2±0.6	–20.0±3.7	–21.0±0.5	–20.5±1.6	–22.9±0.5	–
$PtS + 2\ H_2S_{(aq)} = Pt(HS)_3^- + H^+$	300	500	–	–19.8±2.7	–	–12.5±0.6	–13.6±0.5	–12.0±0.5
$PtS + H_2S_{(aq)} = Pt(HS)_2^0$	300	500	–	–23.1±1.8	–	–5.2±0.5	–7.7±0.5	–7.8±0.5

Uncertainties are equal to the standard deviation for the calculated constants.

Gammons and Bloom (1993) – GB93 (solubility at P_{sat}); Pan and Wood (1994) – PW94 (solubility at P_{sat}); Filimonova et al. (2021) – F21 (density model).

'–' means not available.

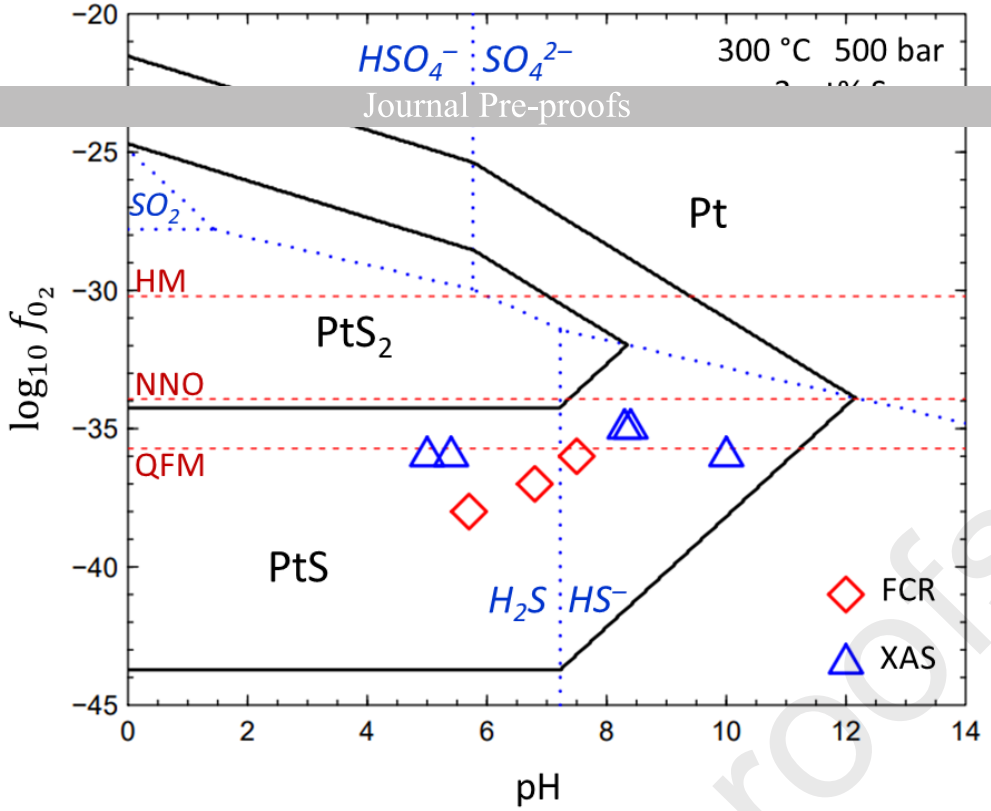

Fig. 1. Phase diagram in the Pt-O-S-H system, at 300 °C/500 bar, and 3 wt% dissolved S, as a function of f_{O_2} and pH. Conventional f_{O_2} mineral buffers are shown as horizontal dashed red lines (HM: Hematite-Magnetite; NNO: Nickel-Nickel Oxide; QFM: Quartz-Fayalite-Magnetite). Predominance boundaries of major sulfur aqueous species are shown by dotted blue lines. Symbols indicate the conditions of our hydrothermal reactor (FCR) and XAS reactor (XAS) experiments in the PtS(s) stability domain.

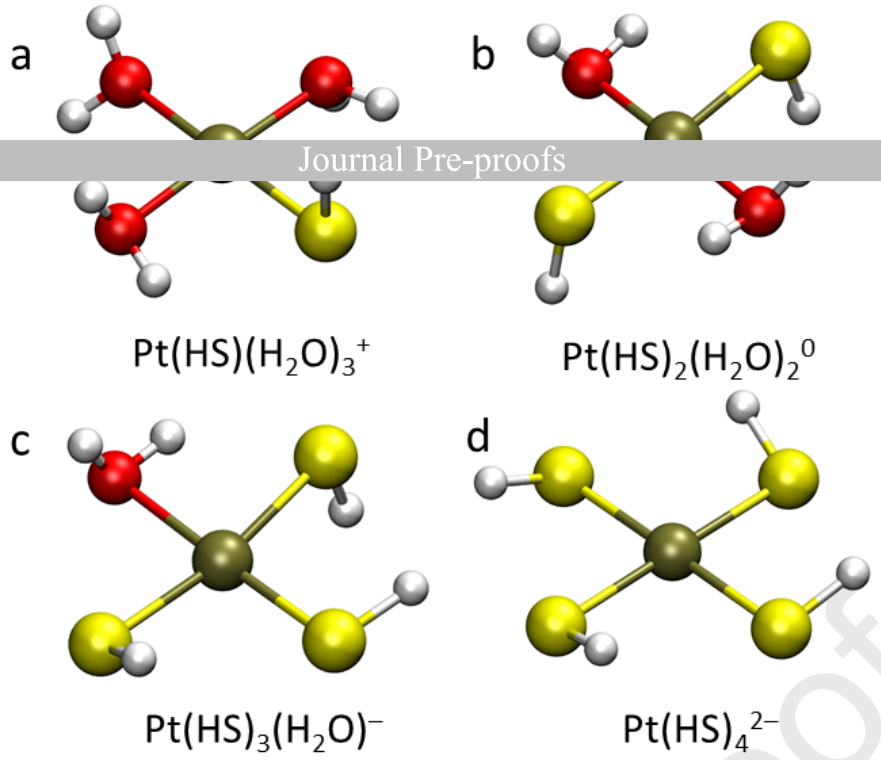

Fig. 2. Ball-and-stick structural presentation of the Pt^{II}-HS-H_2O complexes calculated by DFT (Pt-grey, S-yellow, O-red, H-white). All complexes have a square-planar geometry.

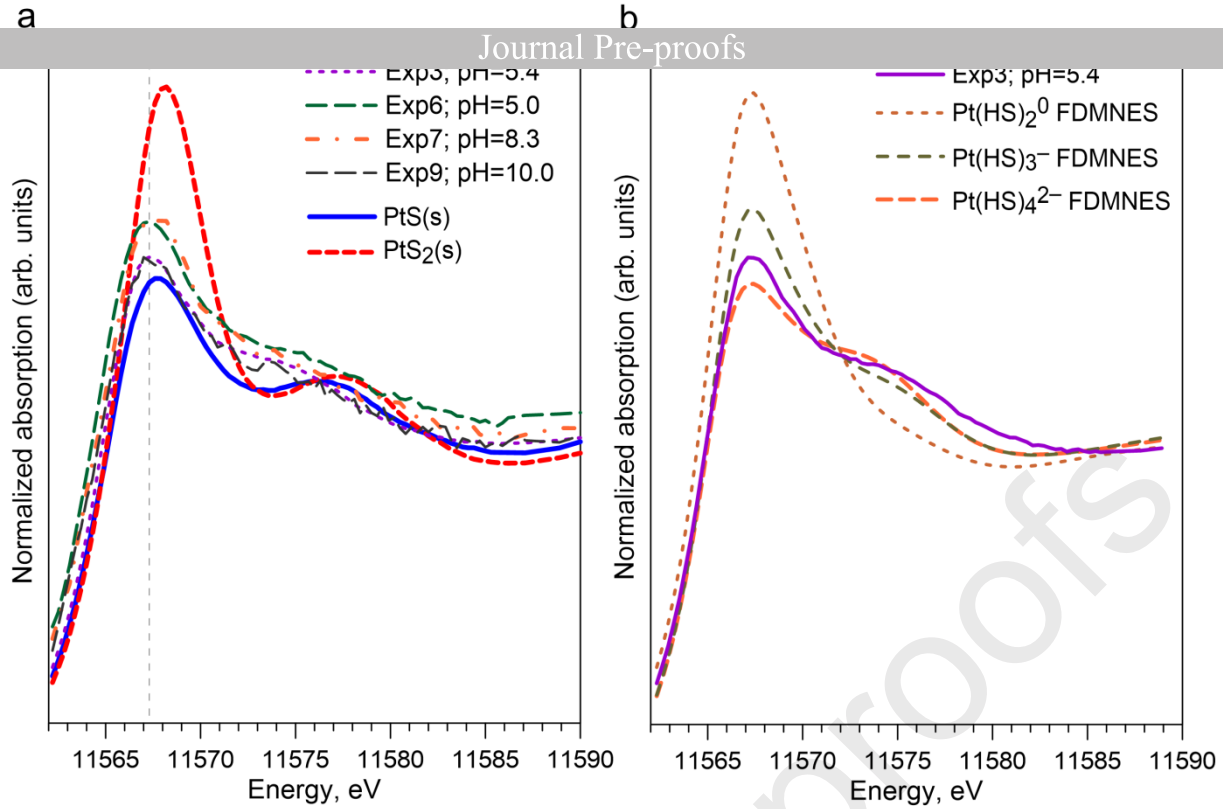

Fig. 3. XANES spectra at the Pt L_{III}-edge of the solid references $Pt^{II}S(s)$ and $Pt^{IV}S_2(s)$, at 25 °C and 1 bar, and of the indicated experimental solutions at 250 or 300 °C, 500 bar **(a)**, and comparison between the spectrum of the thioacetamide solution (Exp3, 250 °C, 500 bar, Table 2) and quantum-chemistry simulated XANES spectra of the three major Pt-HS complexes with DFT-optimized geometries **(b)**. The white-line energy position and shape of the $Pt^{II}S(s)$ reference (marked by a vertical dashed line at 11567.5 eV) are similar to those of the experimental solution spectra, as opposed to $Pt^{IV}S_2(s)$. The spectrum from Exp3, as compared to simulated XANES spectra, is best matched by the $Pt(HS)_4^{2-}$ complex.

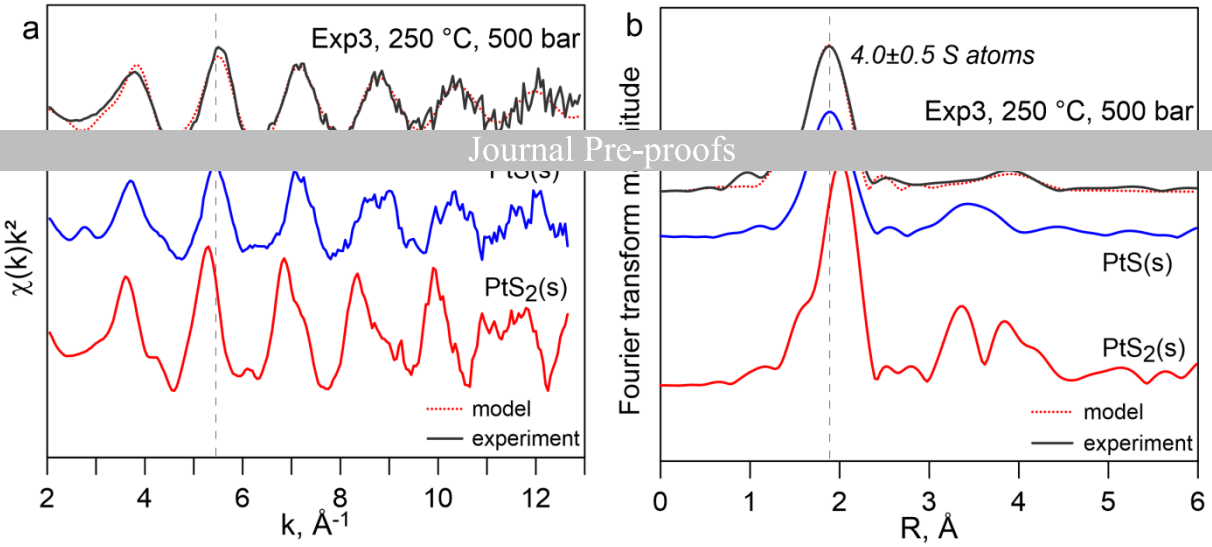

Fig. 4. k²-weighted EXAFS spectra **(a)** and their corresponding Fourier transform magnitudes (not corrected for phase shift) **(b)** of the investigated Pt aqueous solution in experiment Exp3 at 250 °C and 500 bar, and its comparison with the spectra of crystalline references $Pt^{II}S$(s) and $Pt^{IV}S_2$(s) at 25 °C and 1 bar. Dotted curve is least-squares fit to the experimental solution spectrum shown by solid curve. Vertical dashed line is an eye guide to indicate the changes in energy position. The solution spectrum is consistent with 4 S atoms in the 1st shell (S1) and a multiple scattering feature (MS) arising from the square-planar arrangement of S atoms around Pt.

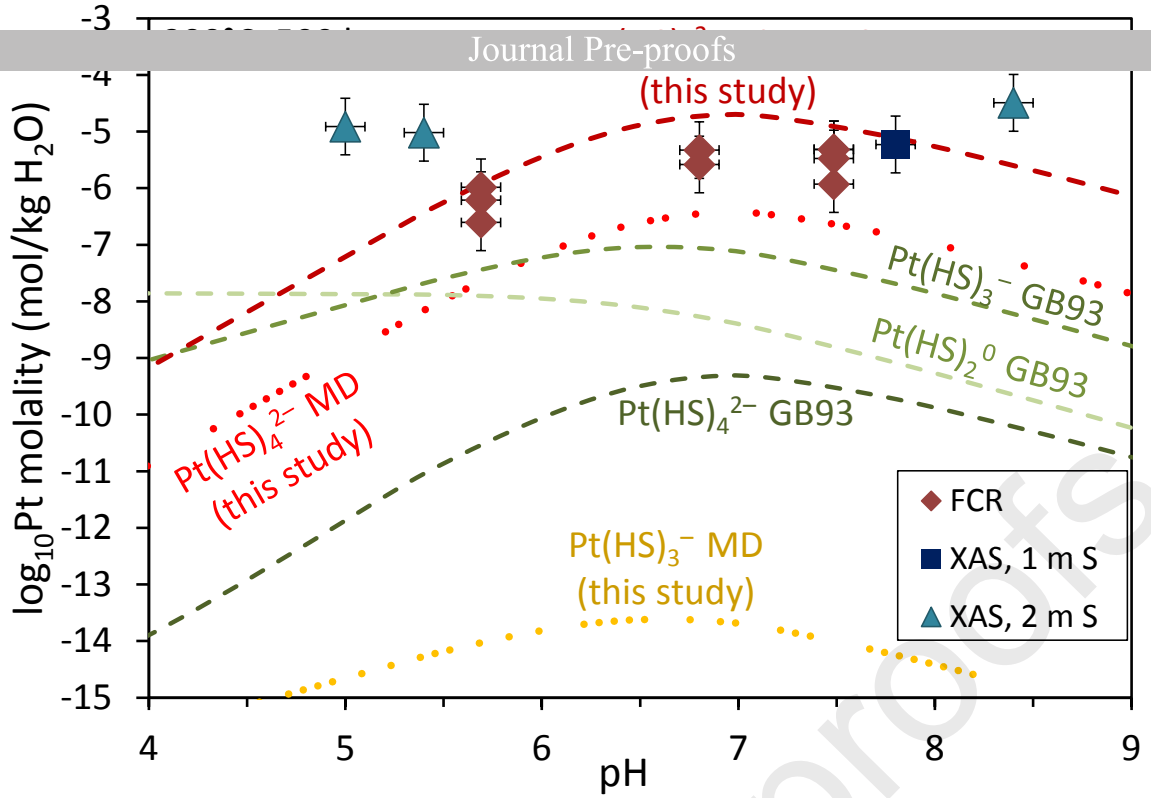

Fig. 5. Platinum dissolved concentrations in equilibrium with PtS(s) in aqueous solution (symbols) as a function of pH at 300 °C and 500 bar measured in hydrothermal reactor experiments (FCR, at 0.7–1.0 m S) and XAS (XAS, at 1 and 2 m S), compared with solubility predictions for the indicated Pt-HS complexes (dotted or dashed curves) using the stability constants from Table 5 derived in this study (FCR+XAS and MD) and Gammons and Bloom (1993) (GB93). All experimental data points were considered in thermodynamic modeling (see Fig. S2a). The sulfur concentration used to calculate the curves was set to 0.90 m S, similar as the concentrations of the FCR and XAS experiments, whereas curves at higher sulfur concentrations (e.g., 2 m S passing through the corresponding XAS datapoints) were omitted to not overload the picture. Note that the concentrations of the $Pt(HS)_2^0$ complex whose constant was predicted by MD in this study are negligibly small ($\log_{10}(Pt(HS)_2^0{}_{MD}) \sim -23$), and not shown here. The $Pt(HS)_4^{2-}$ complex provides the best match of both the experimental solubility data and MD predictions of this study.

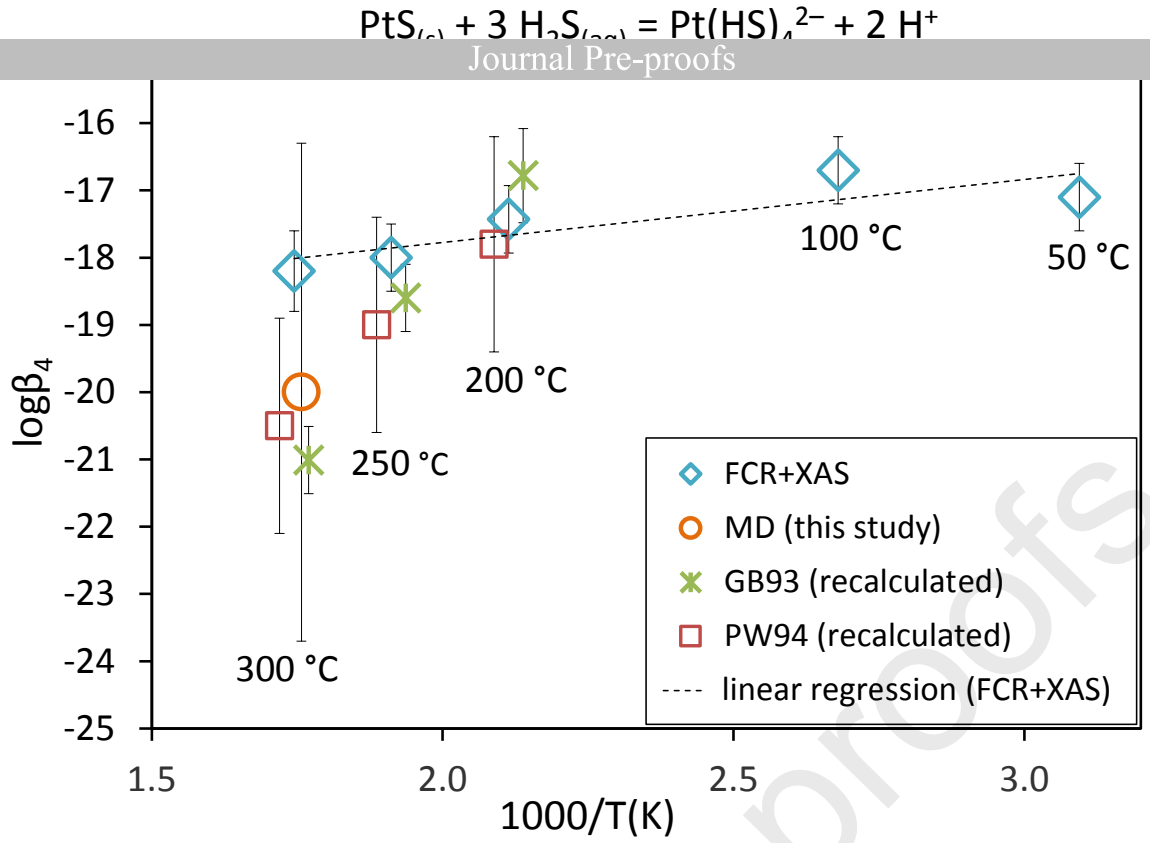

Fig. 6. Values of the reaction constant $\log_{10}\beta_4$: $PtS_{(s)} + 3\ H_2S_{(aq)} = Pt(HS)_4^{2-} + 2\ H^+$, as a function of the reciprocal of absolute temperature 1000/T(K). Data points FCR+XAS were generated from our solubility and least-squares regressed using the linear relationship (dashed line) $\log_{10}\beta_4 = 0.9\times1000/T(K)–19.7$ (±0.5). Other data points, shown in the figure but not used in the regression, are from our FPMD simulations at 300 °C/500 bar (MD) and solubility data of Gammons and Bloom (1993; GB93) and Pan and Wood (1994; PW94) recalculated in this study assuming $Pt(HS)_4^{2-}$ to be the dominant complex. Note that the X-axis position of these data points is slightly shifted to avoid overlap on the graph.

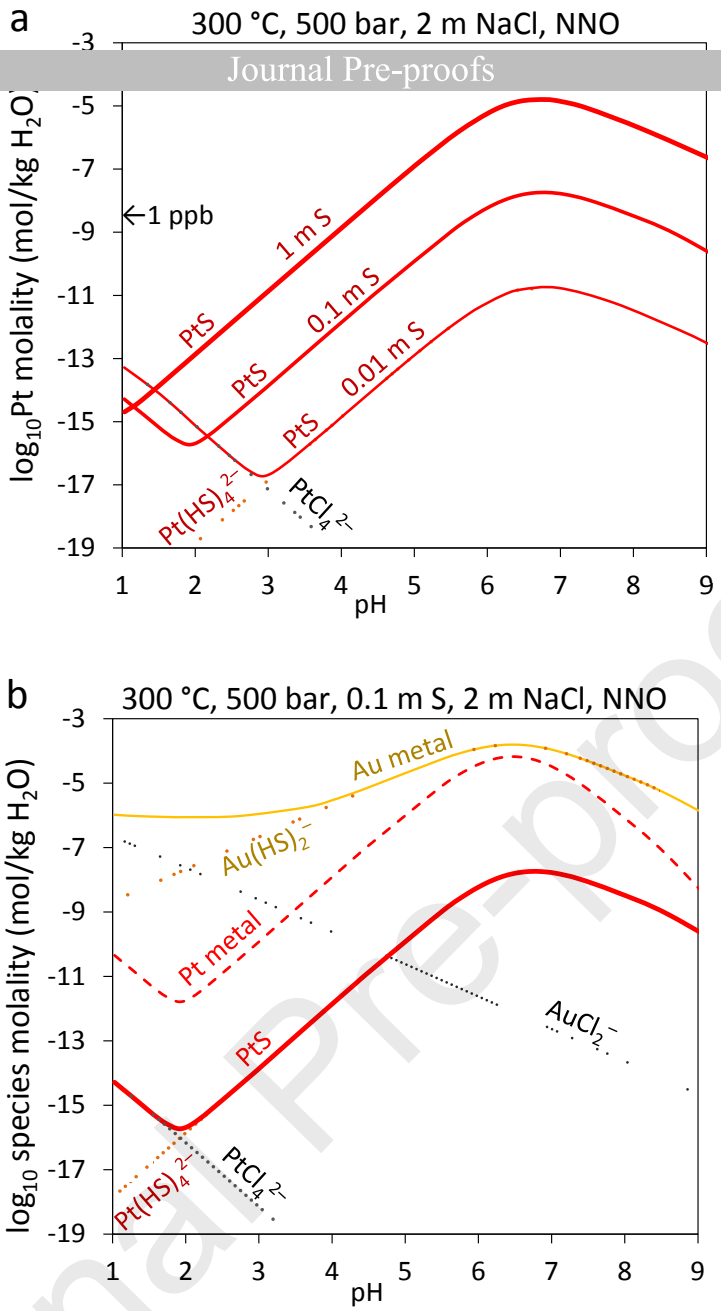

Fig. 7. Solubility of PtS(s) as $Pt(HS)_4^{2-}$ and $PtCl_4^{2-}$ in an aqueous fluid of 2 m NaCl equivalent at oxygen fugacity of the conventional nickel-nickel oxide buffer (NNO, $\log_{10} f_{O_2} = -34$) as a function of pH at the indicated total sulfide concentrations at 300 °C and 500 bar **(a)**. Comparison of the solubility of PtS(s), Pt metal, and Au metal in the same fluid of total sulfide content of 0.1 m, with the indicated Au and Pt species concentrations **(b)**.

Declaration of interests

☒ The authors declare that they have no known competing financial interests or personal relationships that could have appeared to influence the work reported in this paper.

☐The authors declare the following financial interests/personal relationships which may be considered as potential competing interests: